ISSN 0801-9940 No. 02
December 2012

A SEMI-ANALYTICAL MODEL FOR FREE VIBRATIONS OF FREE SPANNING OFFSHORE PIPELINES

by

Håvar Sollund and Knut Vedeld

RESEARCH REPORT
IN MECHANICS

UNIVERSITY OF OSLO
DEPARTMENT OF MATHEMATICS
MECHANICS DIVISION

UNIVERSITETET I OSLO
MATEMATISK INSTITUTT
AVDELING FOR MEKANIKK

DEPT. OF MATH., UNIVERSITY OF OSLO
RESEARCH REPORT IN MECHANICS, No. 2
ISSN 0801-9940 December 2012

A SEMI-ANALYTICAL MODEL FOR FREE VIBRATIONS OF FREE SPANNING OFFSHORE PIPELINES

by

Håvar Sollund and Knut Vedeld

Mechanics Division, Department of Mathematics
University of Oslo, Norway

Abstract. Fast and accurate methods for determining pipeline eigenfrequencies and associated bending stresses are essential to free span design, and hence of great interest to the pipeline industry. The Rayleigh-Ritz approach has been applied in combination with a displacement field taken as a Fourier sine series to obtain a novel, exact semi-analytical solution to an initially curved Euler-Bernoulli beam on a partial elastic foundation subject to axial force. The proposed methodology for calculation of free span eigenfrequencies determines both static and harmonic response with excellent accuracy, and includes nonlinear geometric effects and the pipe stiffening effect caused by static deformation due to gravity. This novel method is easily implemented into a computer program, and the calculation speed is greatly improved compared to traditional FE analyses. Compared to the widely applied semi-empirical formulae of Fyrileiv and Mørk (2002), accuracy is increased and the range of applicability extended. Detailed FE analyses have been carried out to validate the model, and results of the semi-analytical model have also been compared to results obtained using current state-of-the-art engineering practice as defined in Det Norske Veritas' recommended practice provisions DNV-RP-F105 of 2006.

Keywords: Modal analysis, Rayleigh-Ritz, Pipeline, Beam, Initial curvature, Free span.

TABLE OF CONTENTS

1 INTRODUCTION

This report provides solutions for the harmonic response of offshore pipelines on uneven seabeds. Due to seabed unevenness, operational loads and possibly residual lay tension, an offshore pipeline will not touch down on the seabed uniformly along the length of the pipe. The distance between two pipe touchdown points is called a free span. Pipelines are exposed to flow from currents. Depending on the water depth, flow from waves may also be induced at pipe level. Due to the boundary layer between the rough pipe surface and the surrounding flow, vortices are formed and shed off at the lee side of the pipe [Sumer and Fredsøe, 2006; Blevins, 1997]. Vortex formation and shedding create periodically oscillating pressure differentials in in-line and cross-flow directions. Oscillating pressure differentials in in-line direction occur at twice the vortex shedding frequency, and at the vortex shedding frequency in cross-flow direction [Sumer and Fredsøe, 2006].

As span lengths increase, the natural frequencies decrease. Depending on the flow velocity (or vortex shedding frequency) pipelines start to oscillate when the frequency of loading from oscillating pressure differentials approaches the natural frequency. If resonance is achieved, the resulting vibrations may threaten pipeline integrity, either by accumulated fatigue due to long term cyclic loading or local buckling of the pipe from combined static and dynamic loading. Therefore, free spans and fatigue due to vortex induced vibrations (VIV) is an important design aspect in pipeline engineering. For example, subsea pipelines in the Cook inlet in South Alaska experienced 14 failures due to VIV between 1965 and 1976, and the Ping Hu pipeline in the East China sea failed at two locations during the autumn of 2000 due to VIV [Fyrileiv et al., 2005].

The Strouhal law states that the vortex shedding frequency increases linearly, directly proportionally to the velocity of flow [Sumer and Fredsøe, 2006]. Hence, if the lowest natural vibration frequency of the pipeline is higher than twice the maximum vortex shedding frequency, vortex induced vibrations will not occur. If utilized in design, this principle is called an onset criterion [DNV-RP-C205, 2010]. Modern design codes, such as Det Norske Veritas' recommended practice provisions “Free Spanning Pipelines”, DNV-RP-F105 [2006], generally allow for vortex induced vibrations to occur provided that accumulated fatigue damage and peak environmental loading are kept within the confines of acceptable risk for pipeline failure.

For onset, fatigue and peak environmental loading calculations, accurate estimation of in-line and cross-flow natural frequencies of the pipeline is essential. During pipeline design and operations engineering, detailed finite element (FE) modeling of each individual free span is tedious, expensive and often not feasible, however. For this reason DNV-RP-F105 has introduced approximate explicit formulae for static and harmonic response to achieve fast and conservative checks for a range of free span scenarios. Cases where the design criteria are violated, or cases not covered by the range of validity of the simplified response calculations of DNV-RP-F105, must be assessed by detailed FE analyses [DNV-RP-105, 2006].

A free spanning pipeline can be modeled as an Euler-Bernoulli beam on partial elastic foundations, where the elastic foundations are introduced only at the free span shoulders (touch-down zones). Hetenyi [1946] solved the equations of motion for a beam on a variable elastic foundation, while Timoshenko [1983] studied deflections of a freely supported beam with initial curvature subject to transverse and axial forces. Hobbs [1986] applied solutions for simpler boundary conditions and adapted boundary condition coefficients to apply for free span scenarios. Fyrileiv and Mørk [2002] used combinations of parametric FE analyses and the solutions of Hobbs to determine more accurate semi-empirical approximations for the harmonic response. Their approach constitutes the current formulations in DNV-RP-F105 [2006], and it includes significantly more details than previous analytical attempts [Choi, 2001]. In addition to the general refinement, the solutions of Fyrileiv and Mørk [2002] also include an approximation of the stiffening effect on the cross-flow fundamental frequency caused by the static deformation from the pipeline weight. Due to buckling or catenary effects, or both, the applicability of the simplified solutions of Fyrileiv and Mørk [2002] are limited to certain ranges of relative free span lengths and compressive axial forces.

To our knowledge no solution for the equations of motion for an initially curved beam on a partial elastic foundation subject to axial force exists. A novel solution to the boundary value problem has been developed in this report. The solution is based on the widely applied Rayleigh-Ritz approach and the displacement assumption is taken as a Fourier sine series, comparable to work done by e.g. Brubak et al. [2007], Brubak and Hellesland [2007a; 2007b; 2008], and Steen et al. [2004, 2008]. Timoshenko [1983] also represented the displacement field by a Fourier sine series when determining the deflection of a freely supported, initially curved beam. The methodology suggested in this report is easily implemented into a computer program and the computed results are in excellent agreement with the results of FE analyses. Compared to the solutions obtained by the Fyrileiv and Mørk method [2002], the accuracy is

improved and the range of applicability is extended. The increase in range of applicability is highlighted by comparisons to the semi-empirical formulae of Fyrileiv and Mørk [2002].

It will be demonstrated that the semi-analytical approach is radically faster than equivalent FE analyses, making the presented methodology highly suitable for parametric studies of free span harmonic analyses. Free span engineering typically involves significant amounts of parametric studies due to variations in free span lengths, soil stiffness, span gaps, levels of effective axial force etc. along a pipeline route. Consequently, solutions that are faster than equivalent FE analyses are highly desirable for free span engineering software programs such as FatFree [2007]. Work by for instance Brubak et al [2007] and others have demonstrated the substantial gains in computational efficiency obtained with semi-analytical solutions based on Rayleigh-Ritz approaches. Such approaches have also found wide applications in engineering practice [Steen (2005) and Steen et al. (2004)].

2 PROBLEM DEFINITION

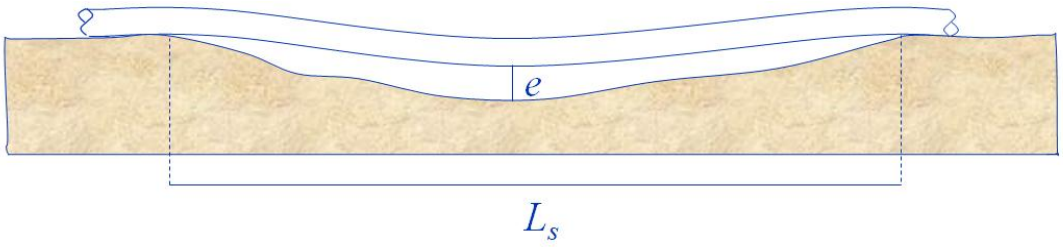

Figure 1 – Pipeline free span scenario. The free span length L_s and the free span gap e are indicated.

Fig. 1 displays a typical pipeline free span scenario. In the figure the span length is L_s and the gap e is the distance between bottom of pipe and the seabed. The gap is typically not uniform along the free span length. According to DNV-RP-F105 [2006], as a single representative value the average gap over the central third of the span is recommended. The pipe has dry mass, including mass of fluid content per unit length m_d, and submerged weight q. For dynamic response calculations one also has to include the effect of the added mass m_a due to acceleration of the surrounding water. The total effective mass m_e is taken as the sum of m_d

and m_a. The added mass increases for decreasing gap [DNV-RP-F105, 2006]. In this report the effective mass of the pipe is taken as an input value and consequently variations in gaps have not been studied explicitly. The regions where the pipe touches down on the seabed are labeled span shoulders, and in the following the length of the shoulders will be denoted $L_{shoulder}$.

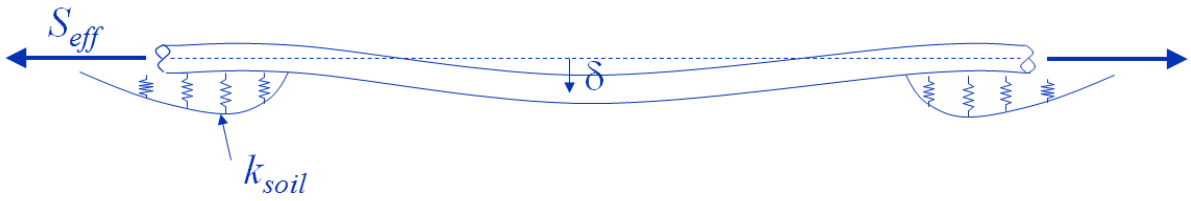

Figure 2 – Static vertical displacement δ at the mid span due to submerged weight and effective axial force S_{eff}.

In Fig. 2 the vertical displacement δ is the static displacement at mid span due to submerged weight and effective axial force. For the purpose of this report, the pipe-soil interaction will be modeled according to DNV-RP-F105 [2006], adopting linear elastic soil stiffness, given as k_{soil} in Fig. 2, but distinguishing between stiffness coefficients for vertical static, vertical dynamic, lateral dynamic, axial static and axial dynamic displacements. The static and dynamic soil spring stiffnesses are termed K_{VS}, K_V, K_L, K_{AXS} and K_{AX} respectively. The effective axial force concept will be applied for calculation of geometric stiffness effects [Sparks, 1983; Fyrileiv and Collberg, 2005]. The effective axial force S_{eff} for an axially unrestrained pipe is zero while the upper bound value, i.e for a a pipe fully restrained axially, [Sparks, 1983; Fyrileiv and Collberg, 2005] is

$$S_{eff} = H_{eff} - \Delta p_i A_i (1-2\nu) - A_s E \Delta T \alpha \quad \textbf{(1)}$$

In Eq. (1) H_{eff} is the residual lay tension, Δp_i is the internal pressure difference relative to internal pressure at the time of laying, A_i is the internal area of the pipe cross-section, A_s is the steel cross-sectional area, E is the Young's modulus, ν is the Poisson's ratio of the steel, ΔT is the change in temperature from the time of laying and α is the temperature expansion coefficient.

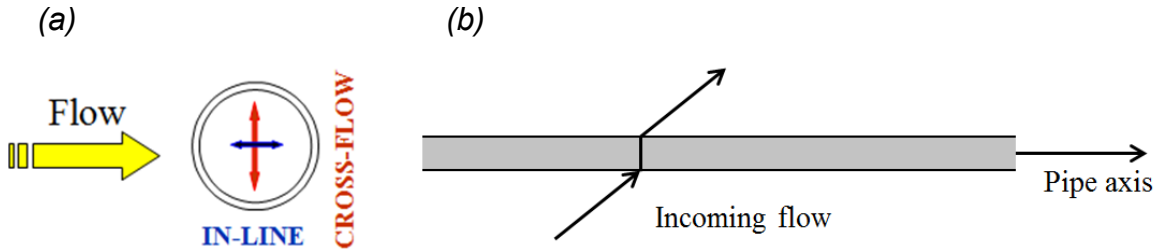

Figure 3 – The in-line and cross-flow directions are defined in the figure, where (a) shows a cross-section of the pipe and (b) shows a plane view of a pipe segment as seen from above.

The in-line direction is perpendicular to the pipe axis and parallel to the flow plane. As illustrated in Fig. 3 the direction of the incoming flow is not necessarily perpendicular to the pipe, however. For a horizontal flow, whether perpendicular to or at an angle with the pipe axis, the in-line direction is horizontal and perpendicular to the pipe axis. The cross-flow direction is perpendicular to both the flow and the pipe axis.

Response frequencies have been assigned subscripts indicating direction and mode number respectively. For instance $f_{IL,2}$ is the frequency of the second in-line mode and $f_{CF,1}$ is the frequency of the fundamental cross-flow mode. Frequencies in-line and cross-flow are equal for a perfectly straight pipe if the lateral and vertical dynamic soil stiffnesses are equal as well. However, the static vertical deflection due to gravity will have a stiffening effect, resulting in an increased cross-flow frequency, particularly for the fundamental mode. Variation in the soil stiffness in-line and cross-flow also results in different harmonic response. Consequently the in-line and cross-flow harmonic responses will be treated separately.

The adopted model applied in the following idealizes the span and seabed geometry to treat discrete free spans. The geometry and boundary conditions for the idealized model is shown in Fig. 4. The shoulders are considered to be horizontal and straight.

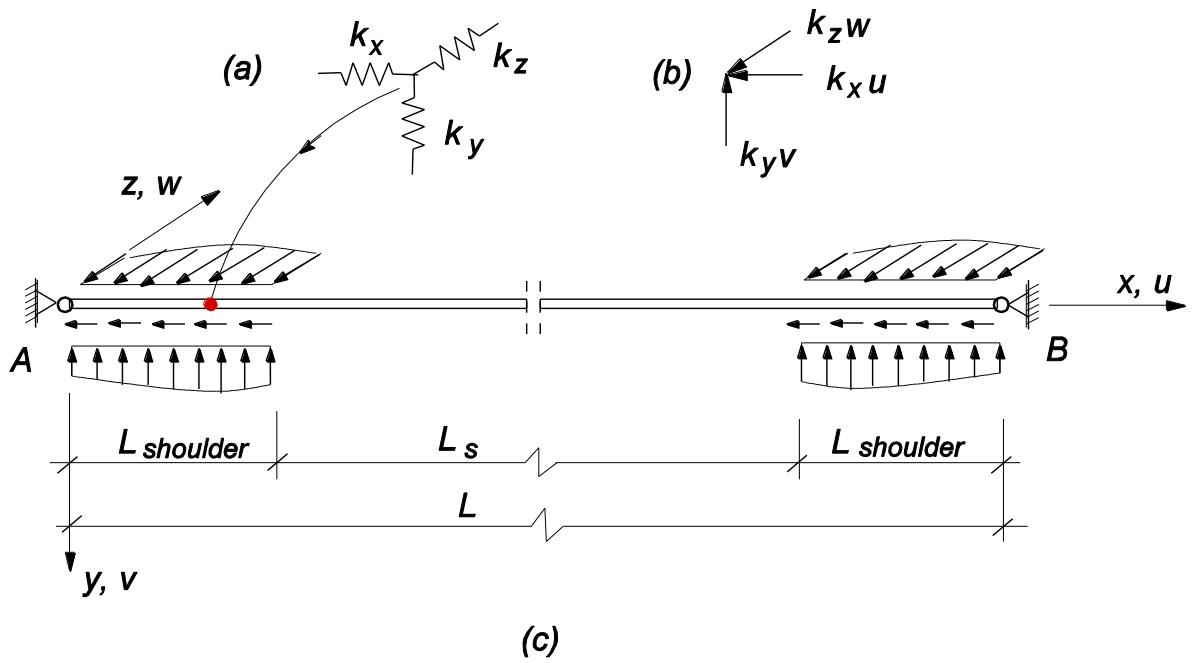

Figure 4 – Definition of pipeline model and Cartesian coordinate system. (a) Static and dynamic soil springs are applied axially, laterally and vertically at the span shoulders. (b) Directions of spring forces. (c) Idealized free span model with boundary conditions.

As seen in Fig. 4 the pipeline ends are assumed to be axially restrained simple supports. This assumption is physically motivated either by span shoulders that are sufficiently long to achieve axial fixity as a result of axial pipe-soil friction, or that other influences from the seabed induces axial fixation (such as neighboring spans, rock dumps, pipe crossings, etc.). The model assumes that there are no additional axial restraints imposed along the span as a result of static deflection, i.e., no global axial translations of the pipe (see e.g. DNV-RP-F110 [2007]) are assumed to feed into the span.

The discrete span models have simple geometries compared to realistic rough seabeds. The model used in the report is a horizontal straight span shoulder, Fig. 2, whereas span shoulders in real conditions may be inclined or curved or both. Some examples of typical span shoulders are shown in Fig. 5. Examples of realistic seabed and span configurations have been reported by Fyrileiv et al. [1998, 2000, 2005].

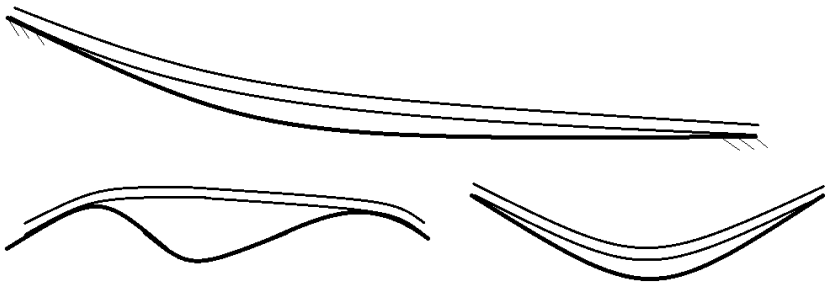

Figure 5 – Three examples of non-straight shoulder configurations for free spans.

In practice shoulder geometry has been shown to have only a small degree of influence on the harmonic response quantities of free spans for in-line response [Mørk et al., 2003]. The static response influences the cross-flow harmonic response however, so the span shoulder geometry may to some extent have an influence on cross-flow response quantities. The effects of span shoulders have not been further discussed in this report and will be investigated in later work instead.

In the following, three solutions to the problem defined by Fig. 4 will be developed:

1. A solution for the static equilibrium case where the pipe is subject to its submerged weight q and effective axial force S_{eff}.
2. A solution to determine the eigenfrequencies, later referred to simply as frequencies, and associated eigenmodes, later referred to as mode shapes, for the linearized harmonic eigenvalue problem in in-line direction subject to pipe effective mass m_e and effective axial force in equilibrium configuration S_{eff}.
3. A solution to determine frequencies and mode shapes for the linearized harmonic eigenvalue problem in cross-flow direction, accounting for the stiffening effect of vertical static displacement, effective mass m_e and effective axial force in equilibrium configuration S_{eff}.

The static solution is carried out first, in order to establish the static configuration and the corresponding value for S_{eff}. The static deflections are only considered to take place in vertical and axial directions. Lateral (in-line) deflections due to static hydrodynamic drag are disregarded in accordance with DNV-RP-F105 [2006]. Consequently, the solutions for in-line frequencies and corresponding mode shapes are affected by the static configuration only in a

limited fashion since S_{eff} in static equilibrium condition is important for the in-line frequencies whereas the geometry is not. The solutions for the cross-flow frequencies and mode shapes, depending on the vertical static deformation configuration as well as its associated level of effective axial force, are performed last.

3 SEMI-ANALYTICAL METHOD

3.1 General Assumptions

To include the effects of static vertical deflections of the model defined in Fig. 4 a curvilinear coordinate system is chosen. The coordinate system is defined in Fig. 6.

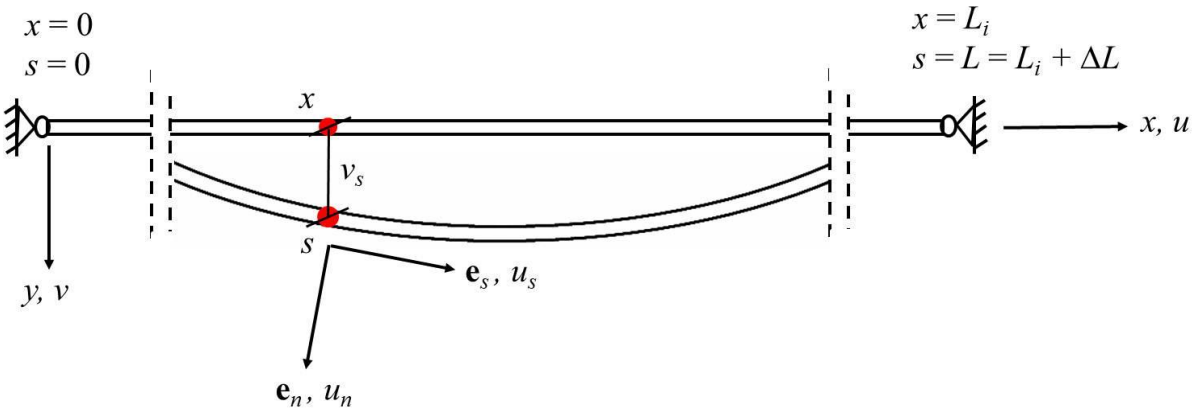

Figure 6 – Curvilinear coordinate system with unit vectors $\mathbf{e}_s$ in the tangential direction and $\mathbf{e}_n$ in the normal direction. The static deflection v_s and the Cartesian coordinate system oriented along the undeformed pipe axis are also shown.

In Fig. 6 $\mathbf{e}_n$ is the direction normal to the pipe axis and $\mathbf{e}_s$ is the direction tangential to the pipe axis. Unlike the *x*,*y*-coordinate system the $\mathbf{e}_s$,$\mathbf{e}_n$-system is not fixed in space, but will rotate along the pipe length ensuring that the $\mathbf{e}_s$ direction is always tangential to the pipe axis. The curvilinear coordinate (or arc length coordinate) *s* denotes the position along the pipe length. The in-plane (either in-line or cross-flow) coordinate directed from the pipe centroidal axis towards the outer circumference is denoted *n*. At each position *s* the displacement in

tangential direction is u_s while the displacement in normal direction is u_n. The radius of curvature $R(s)$ will vary along the pipe length.

For the static solution the initial configuration is straight and for the in-line modal analysis the beam has no deformation in the lateral direction. Consequently the curvilinear coordinate system becomes a standard Cartesian coordinate system for the static solution and the in-line modal analysis. However, for the cross-flow modal analysis (and for the static solution when gravitational loading is applied incrementally), the vertical static deflection configuration rotates the coordinate system resulting in s-dependent radial and tangential unit vectors $\mathbf{e}_n$ and $\mathbf{e}_s$.

Due to the large length-to-diameter ratio Euler-Bernoulli beam theory is assumed to be applicable for modeling of the pipeline, i.e., shear deformations have been disregarded. However, the change in effective axial force due to pipe lengthening which is caused by gravitational loading is included. The following deduction will show how the lengthening is considered in terms of adjusting the effective axial force.

The parametric curve $\mathbf{r}$ describing the position of a point on the beam axis in the deformed configuration can be expressed as follows:

$$\mathbf{r} = \left(x + u_s(x)\right)\mathbf{i} + v_s(x)\mathbf{j} = r_u\mathbf{i} + r_v\mathbf{j} \tag{2}$$

In Eq. (2) u_s is the static deformation in the axial direction and v_s is the static deformation in the vertical direction. The effective axial force is affected by the static loading. If the axial deformation is disregarded, the effective axial force can readily be derived as

$$S_{eff} = S_{eff,i} + \frac{EA}{L_i}\left(\int_0^L \sqrt{1+\left(\frac{dv_s}{dx}\right)^2}\,dx - L_i\right) \approx S_{eff,i} + \frac{EA}{2L_i}\int_0^L \left(\frac{dv_s}{dx}\right)^2 dx \tag{3}$$

In Eq. (3) $S_{eff,i}$ is the initial effective axial force prior to application of static loading and L_i is the model pipe length prior to pipe lengthening. A first order MacLaurin series has been applied to approximate the root and simplify the expression for the arc length integral. Eq. (3) has previously been deduced by Bruschi and Vitali [1991] and others, and provide good predictions for most cases. However, for some cases with very long free spans, it has been determined (from numerical computations) that it is necessary to include also the change in arc length due to the axial displacements, in order to obtain the desired accuracy of computed

frequencies and associated modal stresses. To account for the static axial displacements, the full expression for the arc length integral becomes:

$$S_{eff} = S_{eff,i} + \frac{EA}{L_i}\left(\int_0^L \sqrt{\left(\frac{dr_u}{dx}\right)^2 + \left(\frac{dr_v}{dx}\right)^2}\, dx - L_i \right) \quad \textbf{(4)}$$

By inserting for Eq (2), the root term in Eq. (4) can be approximated as follows:

$$\sqrt{\left(\frac{dr_u}{dx}\right)^2 + \left(\frac{dr_v}{dx}\right)^2} = \sqrt{1 + \left(\frac{du_s}{dx}\right)^2 + \left(\frac{dv_s}{dx}\right)^2 + 2\left(\frac{du_s}{dx}\right)} \approx 1 + \frac{\left(\frac{du_s}{dx}\right)^2 + \left(\frac{dv_s}{dx}\right)^2 + 2\left(\frac{du_s}{dx}\right)}{2} \quad \textbf{(5)}$$

The simplifying expression above was obtained by again using a first order MacLaurin series approximation. Inserting Eq. (5) into Eq. (4) yields

$$S_{eff} = S_{eff,i} + \frac{EA}{2L_i} \int_0^L \left[\left(\frac{du_s}{dx}\right)^2 + \left(\frac{dv_s}{dx}\right)^2 + 2\left(\frac{du_s}{dx}\right) \right] dx \quad \textbf{(6)}$$

Due to symmetry of the boundary conditions, see Figure 4, the last integral term above is zero:

$$\int_0^L 2\left(\frac{du_s}{dx}\right) dx = 0 \quad \textbf{(7)}$$

This result can also be obtained by integrating Eq. (7) with the assumed displacement functions defined by Eq. (15). By combining Eqs. (6) and (7), the final approximation for the effective axial force, as applied in this report, becomes

$$S_{eff} = S_{eff,i} + EA \cdot \frac{\Delta L}{L_i} = S_{eff,i} + \frac{EA}{2L_i} \int_0^L \left[\left(\frac{du_s}{dx}\right)^2 + \left(\frac{dv_s}{dx}\right)^2 \right] dx \quad \textbf{(8)}$$

The assumptions for axial deformations and boundary conditions are further discussed in Section 3.7.

It has further been assumed that the static curvature κ can be approximated as follows

$$\kappa(x) = \frac{1}{R(x)} = \frac{\dfrac{d^2 v_s}{dx^2}}{\left(1 + \left(\dfrac{dv_s}{dx}\right)^2\right)^{\frac{3}{2}}} \approx \frac{d^2 v_s}{dx^2} \tag{9}$$

For the cross-flow modal analysis we will need to know the curvature as a function of the arc-length coordinate *s*. This coordinate is related to the Cartesian coordinate *x* through

$$s(x) = \int_0^x \sqrt{1 + \left(\frac{du_s}{d\tau}(\tau)\right)^2 + \left(\frac{dv_s}{d\tau}(\tau)\right)^2}\, d\tau \tag{10}$$

However, because the change in length due to static deflection is very small compared to the total model length, the following relation is assumed valid for calculation of curvatures

$$s \approx x \quad \Rightarrow \quad \kappa(s) = \frac{1}{R(s)} \approx \frac{d^2 v_s}{ds^2} \tag{11}$$

It should further be noted that the total pipe model length L will be modified due to the pipe lengthening, and will thus be given by

$$L = L_i + \Delta L = 2 \cdot L_{shoulder} + L_s \qquad \text{where} \qquad L_s = L_{s,i} + \Delta L \tag{12}$$

for the cross-flow modal analysis, where $L_{shoulder}$ and L_s are defined in Fig. 4 and ΔL is taken from Eq. (8). In line with the assumption in Eq. (11) we will also assume for the calculation of the stiffness matrix **K** in the cross-flow modal analysis that $L \approx L_i$. This relation is exact for the static and in-line modal analyses.

The validity of the assumptions above is implicitly checked by comparing results of the semi-analytical model with results of detailed FE analyses for a large number of cases.

3.2 Governing Equations

In a curvilinear coordinate system, the Euler-Bernoulli beam formulation results in the following basic displacement assumption, as shown in Appendix B

$$
\begin{aligned}
u_s(s,n,z,t) &= u_0(s,t) - n\left[\kappa(s)u_0(s,t) + \frac{\partial v_0}{\partial s}(s,t)\right] \\
u_n(s,n,z,t) &= v_0(s,t) \\
u_z(s,n,z,t) &= 0
\end{aligned}
\tag{13}
$$

In Eq. (13), u_s is the tangential displacement, u_n is the radial displacement and u_z is the out-of plane displacement which will be disregarded in the following. u_0 is the tangential displacement of a point on the centroidal axis and v_0 is the normal displacement of a point on the centroidal axis. The expression for the tangential displacement u_s is based on the assumption that plane sections remain plane, while rigidity in the transverse direction is assumed for the radial displacements u_n. It is further assumed that the beam cross-section is symmetric about both the *n*- and the *z*-axes. The curvature-dependent term (i.e., the first term in the square brackets) in the expression for u_s implies a rotation of the cross-section for a purely longitudinal displacement of a point on the centroidal axis. This constraint on the displacement field is not necessary (and thus omitted by some authors), but quite natural considering the curved geometry of the problem [Charpie, 1991]. A convenient implication of including the curvature-dependent term is that a (negligibly small) term in the shear-strain components of the strain tensor vanishes, and the shear strains thus become identically zero. It should also be pointed out, as described in several textbooks on strength of materials, that unlike what normally is the case for pure bending, the neutral axis and the centroidal axis do not coincide for curved beams [Srivastava and Gope, 2007]. However, for the ranges of pipe diameters and curvatures of interest in the present context, the eccentricity of the neutral axis is so small that it may be ignored. Accordingly, the deviation from a linear bending stress distribution will be small, as will be shown later in Section 3.6.

Consistent with Euler-Bernoulli beam theory, the only non-zero component of the strain tensor is ε_{ss}. The following expression applies, as derived in Appendix B

$$
\varepsilon_{ss} = \frac{1}{1-\kappa n}\left(\frac{\partial u_s}{ds} - \kappa u_n\right) = \frac{1}{1-\kappa n}\left[\frac{\partial u_0}{ds} - \kappa v_0 - n\frac{\partial}{ds}\left(\frac{\partial v_0}{ds} + \kappa u_0\right)\right]
\tag{14}
$$

The displacements u_0 and v_0 are the unknown displacements for which we must solve. The boundary conditions yield that u_0 and v_0 must be zero at positions $s = 0$ and $s = L$. Note that for the static analysis and the in-line modal analysis this corresponds to positions $x = 0$ and $x = L_i$. Thus the following Fourier sine approximation can be applied for u_0 and v_0

$$u_0(s,t)=\sum_{i=1}^{\infty} D_{u,i}\sin\left(\frac{i\pi s}{L}\right)\sin(\omega t)=\mathbf{N}_u\mathbf{D}_u\sin(\omega t)$$
$$v_0(s,t)=\sum_{i=1}^{\infty} D_{v,i}\sin\left(\frac{i\pi s}{L}\right)\sin(\omega t)=\mathbf{N}_v\mathbf{D}_v\sin(\omega t) \quad \textbf{(15)}$$

where

$$\mathbf{N}_u=\mathbf{N}_v=\left[\sin\left(\frac{\pi s}{L}\right)\quad \sin\left(\frac{2\pi s}{L}\right)\quad \ldots\right]$$
$$\mathbf{D}_u^T=\left[D_{u,1}\quad D_{u,2}\quad \ldots\right]$$
$$\mathbf{D}_v^T=\left[D_{v,1}\quad D_{v,2}\quad \ldots\right] \quad \textbf{(16)}$$
$$\mathbf{u}=\begin{bmatrix}\mathbf{N}_u & \mathbf{0}\\ \mathbf{0} & \mathbf{N}_v\end{bmatrix}\begin{bmatrix}\mathbf{D}_u\\ \mathbf{D}_v\end{bmatrix}=\mathbf{ND}$$

In Eq. (15) ω is the angular frequency. Based on the expression for tangential strain in Eq. (14), a differential operator can be determined in the form

$$\mathbf{d}=\begin{bmatrix}d_{u_0} & d_{v_0}\end{bmatrix}=\frac{1}{1-\kappa(s)y}\left[\frac{\partial}{\partial s}-n\frac{\partial}{\partial s}\kappa(s)\quad -\kappa(s)-n\frac{\partial^2}{\partial s^2}\right] \quad \textbf{(17)}$$

Applying Hamilton's principle and disregarding damping, the equations of motion can be derived and expressed by

$$\mathbf{M}\ddot{\mathbf{D}}+\mathbf{KD}=\mathbf{R}(s,t) \quad \textbf{(18)}$$

where

$$\mathbf{M}=\int_0^L m_e\mathbf{N}^T\mathbf{N}ds$$
$$\mathbf{K}_{struc}=E\int_V(\mathbf{dN})^T(\mathbf{dN})dV$$
$$\mathbf{K}=\mathbf{K}_{struc}+\mathbf{K}_g+\mathbf{K}_{soil} \quad \textbf{(19)}$$
$$\mathbf{R}=\int_0^L\mathbf{N}^T\begin{bmatrix}\mathbf{0}\\ q\mathbf{1}\end{bmatrix}ds$$

In Eqs. (18) and (19), **R** represents the load vector due to the submerged weight *q*, as used when calculating the static deformations. It is set to zero when performing in-line and cross-flow modal analyses. The vector **1** is a vector with unit value in all its entries. In Eq. (18),

$\mathbf{K}_{struc}$ is the structural stiffness matrix, $\mathbf{K}_g$ is the geometric stiffness matrix taking the effective axial force into account, and $\mathbf{K}_{soil}$ is the soil stiffness matrix. The soil stiffness matrix, having different in-line and cross-flow stiffness parameters, as well as different stiffnesses for the static and dynamic response, changes between the three different analyses performed.

By inserting for **N** from Eq. (16) into the mass matrix in Eq. (19) and performing the integration, the following diagonal mass matrix is obtained

$$M_{ii} = m_e \frac{L}{2} \tag{20}$$

In order to obtain the stiffness matrix we first introduce the approximation

$$\frac{1}{1-\kappa(s)n} \approx 1 \tag{21}$$

which is valid since the pipeline diameter $D_s << R(s)$ [Wu, 2009]. Furthermore the curvatures must be limited since too large curvatures would lead to local buckling of the pipe. It should be noted, however, that although the curvatures are small, the mid-span deflection may be significant (i.e., in the order of a few times the pipe diameter) for very long free spans.

After inserting for **N** and **d** from Eqs. (16) and (17) into $\mathbf{K}_{struc}$ in Eq. (19), and performing the integration over the cross-sectional area, the structural stiffness matrix can be written on sub-matrix form as

$$\mathbf{K}_{struc} = \begin{bmatrix} \mathbf{K}_{11} & \mathbf{K}_{12} \\ \mathbf{K}_{21} & \mathbf{K}_{22} \end{bmatrix} \tag{22}$$

where

$$\begin{aligned}
\mathbf{K}_{11} &= EA\int_0^L \mathbf{N}_{u,s}^T \mathbf{N}_{u,s} ds + EI\left(\int_0^L \kappa^2 \mathbf{N}_{u,s}^T \mathbf{N}_{u,s} ds + \int_0^L \kappa_{,s}^2 \mathbf{N}_u^T \mathbf{N}_u ds + \int_0^L \kappa\kappa_{,s}\left(\mathbf{N}_{u,s}^T \mathbf{N}_u + \mathbf{N}_u^T \mathbf{N}_{u,s}\right) ds\right) \\
\mathbf{K}_{12} &= -EA\int_0^L \kappa \mathbf{N}_{u,s}^T \mathbf{N}_v ds + EI\left(\int_0^L \kappa \mathbf{N}_{u,s}^T \mathbf{N}_{v,ss} ds + \int_0^L \kappa_{,s} \mathbf{N}_u^T \mathbf{N}_{v,ss} ds\right) \\
\mathbf{K}_{22} &= EA\int_0^L \kappa^2 \mathbf{N}_v^T \mathbf{N}_v ds + EI\int_0^L \mathbf{N}_{v,ss}^T \mathbf{N}_{v,ss} ds \\
\mathbf{K}_{21} &= \mathbf{K}_{12}^T
\end{aligned} \tag{23}$$

In Eq. (23), the subscript "*,s*" denotes differentiation with respect to the variable *s*, for instance $\mathbf{N}_{v,ss}$ is the vector $\mathbf{N}_v$ from Eq. (16) differentiated twice with regard to *s*. Further discussion on the structural stiffness matrix will be given in the next Sections 3.3, 3.4 and 3.5, where different parts of the sub-matrices yield different results depending on whether the analysis is static or modal, in-line or cross-flow. The geometric stiffness matrix $\mathbf{K}_g$ from Eq. (19) is given by [Cook, 2002]

$$\mathbf{K}_g = S_{eff}\int_0^L \begin{bmatrix} \mathbf{0} & \mathbf{0} \\ \mathbf{0} & \mathbf{N}_{v,s}^T\mathbf{N}_{v,s} \end{bmatrix} ds = S_{eff}\begin{bmatrix} \mathbf{0} & \mathbf{0} \\ \mathbf{0} & \mathbf{K}_{gv} \end{bmatrix} \quad \Rightarrow \quad \left(K_{gv}\right)_{ii} = \frac{(i\pi)^2}{L} \tag{24}$$

where S_{eff} is the effective axial force. Small displacements and rotations are inherently assumed in Eq. (24). It should also be noted, as pointed out by Timoshenko [1983], that for a beam with an initial curvature, the initial deflection (i.e., relative to a straight configuration) should be accounted for when calculating the work done by the longitudinal force S_{eff}. However, as implied by Eq. (11), the initial deflections in the static configuration are modest, and for the present study, Eq. (24) has therefore been assumed sufficiently accurate also for the cross-flow direction.

The static and dynamic soil stiffness matrix $\mathbf{K}_{soil}$ is found by

$$\begin{aligned} \mathbf{K}_{soil} &= \begin{bmatrix} \mathbf{K}_{u,soil} & \mathbf{0} \\ \mathbf{0} & \mathbf{K}_{v,soil} \end{bmatrix} \\ &= \int_0^{L_{shoulder}} \begin{bmatrix} k_{soil,A}\mathbf{N}_u^T\mathbf{N}_u & \mathbf{0} \\ \mathbf{0} & k_{soil}\mathbf{N}_v^T\mathbf{N}_v \end{bmatrix} ds + \int_{L_{shoulder}+L_s}^{L} \begin{bmatrix} k_{soil,A}\mathbf{N}_u^T\mathbf{N}_u & \mathbf{0} \\ \mathbf{0} & k_{soil}\mathbf{N}_v^T\mathbf{N}_v \end{bmatrix} ds \end{aligned} \tag{25}$$

In Eq. (25), the soil stiffness k_{soil} takes on different values depending on the analysis or the response type. It is taken as the vertical static soil stiffness K_{VS} in the static analysis, as the lateral dynamic stiffness K_L for the dynamic in-line response, and as the vertical dynamic stiffness K_V for the dynamic cross-flow response. Similarly, $k_{soil,A}$ is either the static axial soil stiffness K_{AXS} or the dynamic axial soil stiffness K_{AX} for the static and dynamic analyses respectively. For convenience the soil stiffness integrals can be rewritten as

$$\mathbf{K}_{soil} = \int_0^{L} \begin{bmatrix} k_{soil,A}\mathbf{N}_u^T\mathbf{N}_u & \mathbf{0} \\ \mathbf{0} & k_{soil}\mathbf{N}_v^T\mathbf{N}_v \end{bmatrix} ds - \int_{L_{shoulder}}^{L_{shoulder}+L_s} \begin{bmatrix} k_{soil,A}\mathbf{N}_u^T\mathbf{N}_u & \mathbf{0} \\ \mathbf{0} & k_{soil}\mathbf{N}_v^T\mathbf{N}_v \end{bmatrix} ds \tag{26}$$

The length of the span shoulders may influence the results of the static and dynamic analyses if set to be too short. Therefore, the span length is included in the analyses as a fraction of the total model length

$$L_s = cL \quad \Rightarrow \quad L_{shoulder} = \frac{L(1-c)}{2}, \quad 0 < c < 1 \tag{27}$$

This conveniently allows variations of relative shoulder lengths to be considered in later analyses.

Note that despite the pipe lengthening described previously (Eq. (8)), a constant value has been applied for the total pipe model length L (i.e., the initial pipe length L_i is not updated after performing the static analyses) as described in Section 3.2.

Inserting Eq. (16) for $\mathbf{N}_u$ and $\mathbf{N}_v$, as well as Eq. (27) for L_s and $L_{shoulder}$, into Eq. (26) and subsequently performing the integrations, yields the following entries in the soil stiffness matrix:

$$\left(K_{v,soil}\right)_{ij} = \begin{cases} \dfrac{L \cdot k_{soil}}{2}\left[(1-c) - \dfrac{1}{\pi i}\left(\sin\left(\dfrac{i\pi(1+c)}{2}\right)\cos\left(\dfrac{i\pi(1+c)}{2}\right) - \sin\left(\dfrac{i\pi(1-c)}{2}\right)\cos\left(\dfrac{i\pi(1-c)}{2}\right)\right)\right], & i = j \\ \dfrac{L \cdot k_{soil}}{2\pi}\left[\dfrac{\sin\left(\dfrac{(i-j)\pi(1+c)}{2}\right)}{i-j} - \dfrac{\sin\left(\dfrac{(i+j)\pi(1+c)}{2}\right)}{i+j} - \dfrac{\sin\left(\dfrac{(i-j)\pi(1-c)}{2}\right)}{i-j} + \dfrac{\sin\left(\dfrac{(i+j)\pi(1-c)}{2}\right)}{i+j}\right], & i \neq j \end{cases} \tag{28}$$

$$\left(K_{u,soil}\right)_{ij} = \frac{k_{soil,A}}{k_{soil}}\left(K_{v,soil}\right)_{ij}$$

The load vector is relevant in the static analysis only, and the submerged weight is assumed to be the only load to influence the load vector since the effective axial force is included via the geometric stiffness matrix. Consequently, the load vector for the static analyses becomes

$$\mathbf{R} = \begin{bmatrix} \mathbf{R}_u \\ \mathbf{R}_v \end{bmatrix} \quad \text{where} \quad \left(R_u\right)_i = 0 \quad \wedge \quad \left(R_v\right)_i = \frac{qL}{i\pi}\left(1 - \cos(i\pi)\right) \tag{29}$$

With respect to Eq. (19), all quantities have been calculated explicitly with the exception of the integrations over the structural stiffness terms in Eq. (23). How the stiffness terms from Eq. (23) are treated depends on whether a static, lateral dynamic or vertical dynamic analysis is performed. The solutions of the stiffness sub-matrices in Eq. (23) are treated in the next section.

3.3 Static Analysis

In the static analysis the pipe configuration is initially straight, after which weight is applied to the pipe. Since the initial pipe configuration is straight Eq. (23) simplifies to

$$\begin{aligned}
&\mathbf{K}_{11} = EA\int_0^L \mathbf{N}_{u,s}^T \mathbf{N}_{u,s} ds \quad \Rightarrow \quad \left(K_{11}\right)_{ii} = EA\frac{\left(i\pi\right)^2}{2L} \\
&\mathbf{K}_{22} = EI\int_0^L \mathbf{N}_{v,ss}^T \mathbf{N}_{v,ss} ds \quad \Rightarrow \quad \left(K_{22}\right)_{ii} = EI\frac{\left(i\pi\right)^4}{2L^3} \\
&\mathbf{K}_{12} = \mathbf{K}_{21} = \mathbf{0}
\end{aligned} \tag{30}$$

The effective axial force will have an initial level that depends on the global distribution of axial forces over the pipe length, taken either as a conservative maximum from Eq. (1) or more accurately from a detailed global FE analysis. The static deformation of the pipe into the free span will result in an increase in pipe tension due to an elongation of the pipe, as described by Eq. (8). If the effective axial force level is known from FE analyses, a simple linear static analysis is sufficient to give an excellent prediction of the static deformation configuration. In that case, S_{eff} is taken from FE analyses and the equations of motion become linear, i.e., Eq. (24) can be calculated directly. In the cases where it is desirable to calculate the change of effective axial force as a result of vertical static deflection, and implement Eq. (8) into the geometric stiffness matrix, the equation for the geometric stiffness matrix becomes non-linear. The reason for the non-linearity becomes apparent by examining the geometric stiffness term of the energy equations, in which the displacement vector becomes a fourth power expression. The work H_g done by the effective axial force, inserted for Eq. (3), yields

$$H_g = \frac{1}{2}\int_0^L S_{eff}\left(\frac{dv_s}{ds}\right)^2 ds = \frac{1}{2}S_{eff,i}\int_0^L\left(\frac{dv_s}{ds}\right)^2 ds + \frac{EA}{4L}\int_0^L\left(\frac{dv_s}{ds}\right)^4 ds \tag{31}$$

After application of the principle of minimum potential energy the fourth power term in Eq. (31) gives the displacement vector to the power of three in the equilibrium equations and consequently cannot be solved linearly. In the present report the static solution has been obtained using an iterative approach.

The effective axial force is assumed to be uniformly distributed along the length L of the span model, and consequently S_{eff} is a constant. If $S_{eff,i}$ is less than the critical buckling load P_{cr}, the iteration method is a simple fixed-point iteration as outlined in Fig. 7.

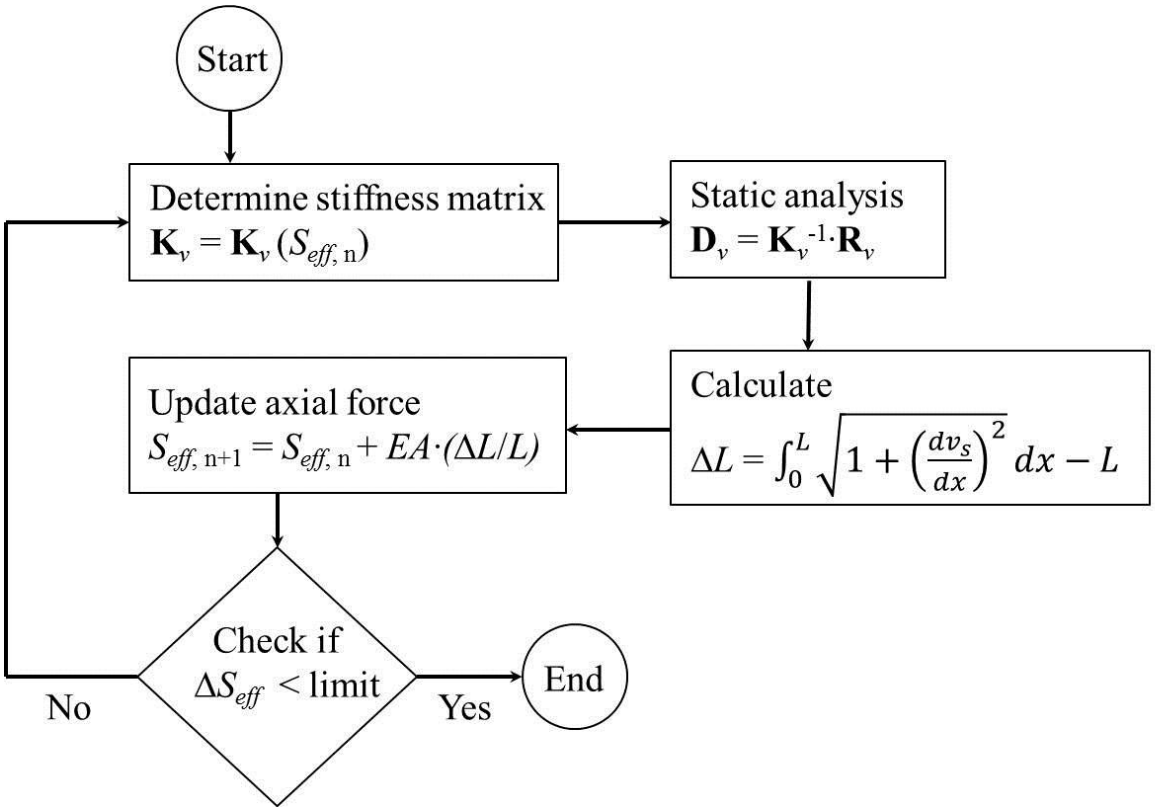

Figure 7 – Flow chart showing calculation of effective axial force when accounting for static deformation.

Since the effective axial force increases with static deflection the first iteration will yield a static deflection which is too high, and since the load is less than P_{cr} a solution for the deflection will exist (but would tend to infinity if P_{cr} is approached). Consequently the correction to S_{eff} will be too large in the second iteration, which will result in a static deflection that is too low. Following this line of thought it is obvious that the solution based on the fixed-point iteration will oscillate around the correct solution, creating an alternating

error term. This leads to the conclusion that the error term is never larger than the difference between two consecutive iteration points. By comparing one term with the next, one may limit the error to any desired accuracy, provided that the compressive axial force applied in the first iteration step is not equal to or larger than P_{cr}. In this case the first step of the solution becomes undetermined.

It should be mentioned that the case of effective axial forces which are higher than the critical buckling load P_{cr} are not realistic. For high pressure, high temperature pipes with very high levels of compressive axial force global buckling of the pipe will normally reduce the overall level of compressive effective axial force to less extreme values. In such cases global FE analyses covering the whole pipeline route are necessary in order to determine the distribution of effective axial forces [DNV-RP-F110, 2007].

For extremely long spans, where cable-like behavior becomes influential, the load must be applied incrementally to achieve a good static equilibrium configuration. In that case, the stiffness matrix and load vector in Fig. 7 must be augmented to include axial displacements and varying curvatures according to Eq. (23).

3.4 In-Line Modal Analyses

The calculation of the structural stiffness matrix is significantly simplified for in-line modal analyses. Here axial and lateral displacements are fully decoupled and the curvatures are zero since the applied weight does not introduce deflections in the in-line direction. Consequently, the structural stiffness expression given by Eq. (23) simplifies to

$$\left(K_{22}\right)_{ii} = EI\,\frac{(i\pi)^4}{2L^3} \tag{32}$$

The full expression for the free vibration problem in-line is thus the general eigenvalue problem

$$\left(\left(\mathbf{K}_{22} + \mathbf{K}_{gv} + \mathbf{K}_{v,soil}\right) - \omega^2 \mathbf{M}_{22}\right)\mathbf{D}_e = 0 \tag{33}$$

Eq. (33) shows that only transverse displacements need to be considered, in accordance with technical beam theory, when the beam is not initially curved.

However the mass matrix **M** is a diagonal matrix which can be expressed as

$$\mathbf{M} = m_e \frac{L}{2} \mathbf{I} \tag{34}$$

where **I** is the identity matrix. Consequently the general eigenvalue problem in Eq. (33) can be rewritten as a special eigenvalue problem

$$\mathbf{K} - \lambda \mathbf{I} = 0 \tag{35}$$

Here **K** is the sum of the structural, geometric and soil stiffness matrices, and λ is given by

$$\lambda = \omega^2 m_e \frac{L}{2} = \frac{f^2 m_e L}{8\pi^2} \tag{36}$$

where f is the frequency.

3.5 Cross-Flow Modal Analyses

In the cross-flow modal analyses, the deformed configuration of the pipeline has an influence on the harmonic response of the pipe. The static deflection causes a coupling between axial and vertical displacements which depends on the magnitude of the static deflection as well as on the axial soil resistance on the shoulders. For the static and in-line modal responses, the sub-matrices of Eq. (23) could be simplified considerably, but for the cross-flow harmonic response the expressions need to include curvature dependent terms. However, several of the terms in Eq. (23) are so small that their contribution to the stiffness matrix may be neglected without loss of accuracy. The terms in Eq. (23) are inversely proportional to powers of the model length L. By ignoring terms in each sub-matrix expression that are two powers of L smaller than the governing term(s), Eq. (23) can be considerably simplified:

$$\begin{aligned}
\mathbf{K}_{11} &= EA\int_0^L \mathbf{N}_{u,s}^T \mathbf{N}_{u,s} ds \\
\mathbf{K}_{12} &= -EA\int_0^L \kappa \mathbf{N}_{u,s}^T \mathbf{N}_{v} ds \\
\mathbf{K}_{22} &= EA\int_0^L \kappa^2 \mathbf{N}_{v}^T \mathbf{N}_{v} ds + EI\int_0^L \mathbf{N}_{v,ss}^T \mathbf{N}_{v,ss} ds \\
\mathbf{K}_{21} &= \mathbf{K}_{12}^T
\end{aligned} \tag{37}$$

In Eq. (37), $\mathbf{N}_u$ and $\mathbf{N}_v$ are given by Eq. (16). With regard to the simplified expressions given by Eq. (37), it is pointed out that the terms that have been disregarded are exactly those terms that were introduced due to the curvature-dependent term in the expression for the tangential displacement u_s in Eq. (13).

The curvature κ is determined from the static deflection as described by Eq. (11). The expression for κ becomes

$$\kappa = -\left(\frac{\pi}{L}\right)^2 \sum_{a=1}^{n} D_{static,a} \cdot a^2 \sin\left(\frac{a\pi s}{L}\right) \qquad \textbf{(38)}$$

where n is the number of sine terms included in the expression for vertical displacements v_0. Consequently, κ is a function in s with coefficients D_{static} determined in the static analysis. Explicit expressions for each sub-matrix in Eq. (37) may be established. These are deduced and presented in detail in Appendix A.

The numerical calculation of the matrices given in Eq. (37) involves integrals of sums and double sums of products of up to 4 trigonometric functions. Each product of three or four trigonometric functions can be transformed into sums of three or four trigonometric terms. If performed directly, these trigonometric integrals (over indexes i, j, a and b) are conducted at $O(n^4)$ flops. The eigenvalue solver used for calculating frequencies and associated eigenvectors operates at $O(n^2)$ flops, which makes the generation of the stiffness matrix much slower than the calculation of eigenvalues. To overcome this problem a "combinatoric" solution, utilizing band patterns in the stiffness sub-matrices, was adopted for the integrations in Eq. (37). This reduces the calculation of the stiffness matrix to $O(n^2)$ flops. The development of the "combinatoric" solution is shown in Appendix A.

After establishing the correct structural stiffness matrix the eigenvalue problem may be written on the form presented by Eqs. (33) and (35), but now including the axial displacement and coupling components which could be left out in the in-line modal analyses. Since the mass matrix is still diagonal the problem may be solved as a special eigenvalue problem, in the same manner as in the in-line harmonic analysis.

3.6 Calculation of Secondary Quantities

Primary results such as frequencies and mode shapes are presented in Sections 6.1 and 6.2. The frequencies are described by Eq. (36), and the mode shapes can be derived from the associated eigenvectors from the eigenvalue predictions as follows

$$\varphi_{IL/CF,j}(s) = v_{0,j} = \frac{\sum_{i=1}^{n} (\mathbf{D}_e)_i \sin\left(\frac{i\pi s}{L}\right)}{\max_{0\le S\le L} \sum_{i=1}^{n} (\mathbf{D}_e)_i \sin\left(\frac{i\pi s}{L}\right)} \tag{39}$$

In Eq. (39) $\varphi_{IL,j}$ is the j-th mode shape calculated from the eigenvector $\mathbf{D}_e$ corresponding to the j-th in-line frequency. Similarly $\varphi_{CF,j}$ is the j-th cross-flow mode shape. Based on the mode shapes unit diameter stress amplitudes can then be calculated according to DNV-RP-F105 [2006] from

$$\sigma_{ss,j} = A_{IL/CF} = DE\left(\frac{D_s - t_s}{2}\right)\frac{d^2\varphi_j}{ds^2}\left(1+\left(\frac{d\varphi_j}{ds}\right)^2\right)^{-3/2} \tag{40}$$

In Eq. (40) $\sigma_{ss,j}$ is the j-th modal stress amplitude for either in-line or cross-flow direction, and t_s is the steel wall thickness of the pipe. The unit diameter stress amplitude is multiplied by a factor D based on the assumption that the mode shape φ_j has been normalized to unit amplitude. Generally, based on Eq. (14), the unit diameter modal stress can be expressed by

$$\begin{aligned} &\sigma_{ss,j} = DE\frac{1}{1-\kappa_j n}\left(\left[\frac{du_{0,j}}{ds} - \kappa_j v_{0,j} - n\frac{d}{ds}\left(\frac{dv_{0,j}}{ds} + \kappa_j u_{0,j}\right)\right]\right), \\ &n = -\frac{D_s - t_s}{2} \end{aligned} \tag{41}$$

In Eq. (46) the stress is observed to include axial and curvature dependent terms. Based on the cases studied in this report two of the terms have been found to be negligible, leading to

$$\frac{1}{1-\kappa_j n} \approx 1, \quad n\frac{d}{ds}\left(\kappa_j u_{0,j}\right) \approx 0 \tag{42}$$

The remaining differences between Eqs. (40) and (41) include terms that yield axial stresses that are constant over the pipe cross-section. Such stresses are not included in fatigue and

extreme environmental loading calculations according to DNV-RP-F105, and are therefore not part of present industry practice. As a result, these contributions have not been assessed.

The remaining secondary quantities assessed in this report are the effective axial force for the static configuration and the maximum static deflection due to gravity. The effective axial force is calculated according to Eq. (8), and the maximum static deflection as follows

$$\delta = \max_{0\le s\le L}\left(\sum_{i=1}^{n} D_{static,i}\sin\left(\frac{i\pi s}{L}\right)\right) \tag{43}$$

3.7 Axial Soil Stiffness and Choice of Boundary Conditions

Pipelines are long and normally include several free span areas. The global behavior of the pipeline will govern the effective axial forces. Consequently, there is no simple approach to determine a local model which will include global effects of effective axial force on a local span. This report does not attempt to solve the problem of identifying a suitable local boundary condition to accommodate for global pipeline behavior, which leaves the following discussion of boundary condition a convenient approach for the time being but first and foremost a choice which will allow for validation of the semi-analytical model. The boundary condition is aligned with the approach in DNV-RP-F105 [2006] in order to make comparative studies as relevant as possible.

The total length L of the free span model and the static axial soil stiffness K_{AXS} will influence cross-flow harmonic response directly due to the axial coupling between vertical and axial displacements in the static equilibrium configuration, as seen from Eq. (37). The effective axial force will also be a function of L and K_{AXS}, which influences both the in-line and the cross-flow harmonic responses, as indicated by Eqs. (19) and (24). It could be argued that the model length should be increased until the accumulated axial friction reaches the initial effective axial force level near the model boundaries. This procedure would make the span response independent of the model length. The static axial friction between the pipe and the seabed is, however, not very high when compared to the often large values of effective axial forces. Consequently the necessary mobilization length of the accumulated axial friction is significant in most cases, in terms of accounting for the change in length of a pipe due to static deflection. Since the required mobilization lengths are so large an idealized free span model (with horizontal, straight shoulders) would no longer be representative of a realistic

free span scenario. This is because a length-independent model would make assumptions not only of the span, but also of a large area surrounding the span. In reality spans may have neighboring spans, and the seabed geometry will vary, with the occurrence of both inclined and curved span shoulders. A neighboring span may for instance act as an axial fixation if it has a comparable length to that of the considered span. Thus it is reasonable to assume that in most cases the pipe will be axially restrained closer to the free span than the mobilization length of the axial friction would suggest. More realistic span scenarios have been reported elsewhere, for instance by Fyrileiv et al. [1998].

A model with flat span shoulders and fixed shoulder lengths equal to three times the span length has been chosen. No axial friction is incorporated when determining the static configuration, but dynamic axial stiffness is included when performing the modal analyses. To align the presented results in this report with current industry practice, the same assumptions have been made regarding model length and axial friction behavior. Note, however, that the semi-analytical model presented here would be equally applicable for determination of natural frequencies and mode shapes on other choices of span shoulder lengths and axial friction behavior.

4 THE FINITE ELEMENT MODEL

The commercially available finite element solution software ABAQUS [2012] was used for finite element modeling. The beam element PIPE31 was used for modeling the pipe. This is a first order shear deformable linear beam element. Linear springs were used to model the soil stiffness. The model is generated according to Fig. 4, on page 8, with vertical, lateral and axial springs at each node. Shoulder lengths and span lengths were set to be equally long in the finite element and corresponding analytical models. The analysis procedure for the FE model is as follows

1. Pipe and soil spring elements are generated. The mass of the pipe elements are set to include the total effective mass.
2. The pipe is fixed at one end and all springs are fixed at nodes which do not connect to pipe elements. The other end is temporarily free.
3. Dynamic soil springs are removed from the model

4. $S_{eff,i}$ is applied at the free end of the pipe, constituting the first step of the static analysis.
5. The free end (i.e., the loaded end) of the pipe is subsequently fixed.
6. Submerged weight is applied as a distributed vertical load. This constitutes the second step of the static analysis.
7. The static springs are removed and the dynamic soil springs are re-introduced strain free.
8. The modal analysis is performed on the static configuration.

Non-linear geometric effects are included in all the steps of the analysis to account for changes in effective axial force from static deflection, and furthermore to allow the modal analysis to base the tangent stiffness matrix on the final deformed configuration as opposed to the initial undeformed configuration.

The recommendation for maximum element lengths in DNV-RP-F105 [2006] is one outer pipeline diameter, i.e., the ratio of the element length to the outer pipeline diameter should be less than 1. In the studies presented in this report, comparisons are made not only between the fundamental modal frequencies but also between static deflections, equilibrium effective axial force levels and frequencies and stresses for higher order modes. The comparisons show that element lengths of 1 outer pipe diameter resulted in good results for the fundamental frequencies, but convergence was not achieved for higher order modal stresses unless element lengths were chosen in the order of 10% of the outer pipe diameter. Consequently an element length equal to 10% of the outer pipe diameter was chosen throughout in the analyses.

5 THE SEMI-EMPIRICAL METHOD OF FYRILEIV AND MØRK

For comparisons and illustrations of range of applicability of the model proposed in this report the analytical semi-empirical model developed by Fyrileiv and Mørk [2002] is used. The range of application for the model is listed below

- $L / D_s < 140$
- $\delta / D < 2.5$
- $S_{eff}/P_{cr} > -0.5$

According to the list of limitations of the model, the relative span length must not exceed 140, the normalized static mid span deflection must not exceed 2.5 and the effective axial force must not exceed half the critical buckling load.

The fundamental in-line and cross-flow frequency of a free span is given by Fyrileiv and Mørk [2002] as

$$f \approx C_1 \sqrt{\frac{EI}{m_e L_{eff}^4}\left(1+\frac{S_{eff}}{P_{cr}}+C_3\left(\frac{\delta}{D}\right)^2\right)} \tag{44}$$

In Eq. (44), C_1 and C_3 are boundary condition coefficients, given by the following equation

$$C_1 = 3.56,\ C_3 = \begin{cases} 0, & in-line \\ 0.4, & cross-flow \end{cases} \tag{45}$$

The effective length concept used above was initially introduced by Netenhyi [1946] and Hobbs [1986], but refined by Fyrileiv & Mørk [2002] using systematic finite element analyses. The effective length L_{eff} is defined in DNV-RP-F105 [2006] by

$$L_{eff} = \begin{cases} \dfrac{4.73L_s}{-0.066\beta^2+1.02\beta+0.63} & \text{for} \quad \beta \geq 2.7 \\ \dfrac{4.73L_s}{0.036\beta^2+0.61\beta+1.0} & \text{for} \quad \beta < 2.7 \end{cases}$$
$$\beta = \log\left(\frac{KL_s{}^4}{EI}\right) \tag{46}$$

In Eq. (46), K is the relevant soil stiffness for the relevant direction and type of displacement, i.e. static or dynamic.

The critical buckling load is defined as

$$P_{cr} = 4\pi^2 EI / L_{eff}^2 \tag{47}$$

This corresponds to the buckling load of a pipe rotationally fixed at ends that are a distance L_{eff} apart.

Further quantities for comparisons are peak unit diameter modal stresses, peak static bending moments, maximum static deflections as well as frequencies and associated peak unit diameter stress amplitudes for higher order modes.

The unit diameter stress amplitude for the fundamental mode, A_{IL} in-line and A_{CF} cross-flow, is the stress associated with a displacement equal to a unit diameter amplitude of the relevant fundamental mode shape. It is obtained by

$$A_{IL/CF} = \max\left(14.1\left(\frac{L}{L_{eff}}\right)^2;\quad 8.6\right)\cdot\frac{D(D_s - t_s)E}{L_{eff}^2} \tag{48}$$

In Eq. (48), the only difference between A_{IL} and A_{CF} stems from the difference in effective length due to different values for the in-line dynamic soil stiffness and the cross-flow dynamic soil stiffness. The peak static bending moment M_{static} is defined as

$$M_{static} = \max\left(\frac{1}{18(L_{eff}/L)^2 - 6};\quad \frac{1}{24}\right)\frac{w_s L_{eff}^2}{1+(S_{eff}/P_{cr})} \tag{49}$$

The peak static deflection (mid-span) is given as

$$\delta = \frac{1}{384}\frac{w_s L_{eff}^4}{EI(1+S_{eff}/P_{cr})} \tag{50}$$

6 RESULTS AND DISCUSSION

6.1 Comparisons with FE Solutions and Validation of the Semi-Analytical Model

Premises for selection of span cases

The main validation of the semi-analytical model is performed by comparing with detailed FE analyses results for 18 different free span cases. The cases have been selected to ensure that some exceed and some do not exceed the range of applicability of the analytical model of Fyrileiv and Mørk [2002] presented in Section 5. The cases that are chosen for comparisons are selected for the purpose of demonstrating that the semi-analytical model is applicable irrespective of span length, static deflection, and level of effective axial forces below the critical buckling load. The methodology described in Section 3 has been implemented in Matlab (2010) and the eigenvalue solver from Matlab was used to determine frequencies and mode shapes.

Prior to presenting results, a discussion on the measurement points for accuracy assessment is considered appropriate. Pipeline engineers may assume different roles when they encounter free span problems. The engineer may for instance be doing pipeline design, pipeline integrity management (in free span design, pipeline integrity management involves the task of continuously monitoring free span development and fatigue damage utilization for an operational pipeline) or verification of either design or integrity management. Design and integrity management of pipelines may be performed at various levels of complexity or degree of details in the industry depending on the phase (concept, FEED or detailed design).

In free span design, the complexity ranges from simplistic design based on onset criteria [DNV-RP-C205, 2010] to advanced fatigue and peak environmental load estimations based on long-term environmental statistics and structural reliability methods [Hagen et al., 2003]. The only structural response parameters that are relevant for onset criteria, the simplest form of free span design, are the fundamental harmonic in-line and cross-flow frequencies. For detailed fatigue calculation assessments, however, it is necessary to determine several harmonic in-line and cross-flow frequencies, and also the associated modal stresses. As described in Sections 3.3 and 3.5, the harmonic frequencies depend on the effective axial force and the cross-flow frequencies depend on the static deformation configuration as well. To cover all the relevant parameters for engineers doing free span design or verification, it is, thus, necessary that the semi-analytical model presented in this report is capable of providing sufficient prediction accuracy of the effective axial force (from static equilibrium), the static deformation configuration, modal in-line and cross-flow frequencies and modal in-line and cross-flow stresses. However, it should be noted that there are numerous inherent uncertainties in the analyses, such as soil stiffness, damping, lay tension etc. These are all important and relevant parameters in an overall reliability study of a free span. The proposed model is suitable for carrying out reliability studies. However, the present study is only concerned with the accuracy of the model for given deterministic input variables.

Results and comparisons

For the purposes of this paper it has been assumed that the accuracy of the model can be sufficiently documented by comparing three in-line and three cross-flow modes for each case, both in terms of frequencies and modal stresses. This leaves us with 6 frequencies, 6 modal stresses, static deflection and equilibrium effective axial force to compare for each validation

case. In other words, 14 parameter comparisons between analytical and FE results has been conducted for each case, resulting in a total of 256 parameter comparisons in total. The total matrix of these results is necessarily very large and time-consuming to read, so the full details are given in Appendix C. For the purpose of the discussion, two of the 18 verification cases will be examined in some detail. The two selected cases correspond to case 1 and case 16 in Appendix C. The relevant input parameters are given in Table 1, whereas the results from both FE analyses and calculations with the semi-analytical method are presented in Table 2.

Table 1- Input data for verification cases 1 and 16

Span:	**Case 1**	**Case 16**	**Unit**
L_s	125	50	m
$L_{shoulder}$	375	150	
L_{elem}	0.1	0.01683	
Soil data:			
K_{VS}	$1.3 \cdot 10^6$	$1.35 \cdot 10^6$	N/m^2
K_V	$1.20 \cdot 10^7$	$3.06 \cdot 10^7$	
K_L	$8.29 \cdot 10^6$	$2.30 \cdot 10^7$	
K_{AX}	$8.29 \cdot 10^6$	$2.30 \cdot 10^7$	
Pipe:			
D_s	1	0.1683	m
t_s	0.03	0.0183	m
q	5539	664.1	N/m
m_e	2178	90.5	kg/m
$S_{eff,i}$	0	$-2.5 \cdot 10^4$	N
E	$2.07 \cdot 10^{11}$		N/m^2
v	0.3		-

The two cases presented in Tables 1 and 2 differ in several important ways. Case 1 represents a quite typical and realistic free span scenario, where the span length and mid-span deflection both are within the parameter validity ranges listed in Section 5 for the semi-empirical model by Fyrileiv and Mørk [2002]. In addition, there is no initial effective axial force in this case. Case 16 on the other hand, has a very large relative span length of $L_s/D_s \approx 300$ and large relative mid-span deflections of $\delta/D > 5$. On top of this, a compressive axial force of 25 kN is applied initially. This corresponds to approximately 0.4 times the critical buckling load (calculated according to Eq. (47)). Hence, case 16 represents a very challenging free span configuration far outside the range of validity of the approximate response methodology presented by Fyrileiv and Mørk and adopted in DNV-RP-F105. For such spans, detailed assessment by means of for instance FE modeling is normally required in order to determine

important response quantities such as natural frequencies and stress amplitudes with sufficient accuracy. Thus, case 1 represents a span configuration where the semi-analytical methodology we have presented here should give results that are consistent with FE results with a high degree of accuracy, while case 16 is interesting because it exceeds the range of validity of the model by Fyrileiv and Mørk by more than a factor of 2 on span length and mid-span static deflection.

Table 2 – Comparison of results from FE and semi-analytical model for verification cases 1 and 16

Result	Unit	Case 1			Case 16		
		FE	Analytical	Ratio	FE	Analytical	Ratio
$f_{IL,1}$	Hz	0.220	0.221	1.006	0.542	0.541	0.998
$f_{IL,2}$		0.567	0.571	1.006	1.219	1.221	1.000
$f_{IL,3}$		1.049	1.082	1.032	2.109	2.114	1.003
$f_{CF,1}$		0.370	0.371	1.000	1.223	1.224	1.001
$f_{CF,2}$		0.577	0.579	1.002	1.534	1.527	0.995
$f_{CF,3}$		1.074	1.107	1.031	2.167	2.172	1.002
$A_{IL,1}$	MPa	126.5	127.5	1.008	33.0	32.94	0.997
$A_{IL,2}$		303.4	308.7	1.018	77.6	77.32	0.997
$A_{IL,3}$		603.0	605.9	1.005	134.3	133.8	0.997
$A_{CF,1}$		159.0	158.3	0.996	79.2	78.8	0.995
$A_{CF,2}$		324.7	323.7	0.997	102.6	99.8	0.973
$A_{CF,3}$		602.0	633.3	1.052	97.9	98.7	1.008
S_{eff}	N	$1.51 \cdot 10^6$	$1.51 \cdot 10^6$	1.000	$1.60 \cdot 10^5$	$1.58 \cdot 10^5$	0.986
δ/D	-	2.04	2.04	1.000	5.31	5.28	0.994
Comp. Time	s	112.1	0.21	533.8	243.0	16.98	14.31

From the results presented in Table 2, it is clear that there are very small differences between the FE and semi-analytical results for case 1. In fact, for 10 of the 14 compared parameter values, the relative differences are below 1%, while the maximum relative difference is 5.2% for the unit diameter stress amplitude of the third cross-flow mode. In comparison, the semi-empirical method by Fyrileiv and Mørk predicts fundamental in-line and cross-flow frequencies of 0.225 and 0.341, respectively, corresponding to relative differences of approximately 2% and 8%. Interestingly, the accuracy of the semi-analytical model is equally good for case 16 as for case 1. Despite the very large values of relative length and mid-span deflection, the maximum relative difference between the FE and semi-analytical results is 2.7% for the unit diameter stress amplitude of the second cross-flow mode. This suggests that the semi-analytical model has no limitation of accuracy even for extremely long spans. The

longest span investigated in the 18 comparative cases, is that of case 18 with L_s/D_s = 356 (see Appendix C). As can be seen in Table C.3, even for this case there are no notable differences between the results of the semi-analytical model and the FE solutions. Note from Table 2 and Appendix C the increase in computational time between case 1 and the cases 16 and 18. This demonstrates that the non-linearity of the problem introduces some reduction in the computational efficiency of the semi-analytical model compared to FE solutions. In reality, spans with relative length ratios L_s/D_s in the range of 300 are highly uncommon, however.

The accuracy of the semi-analytical model may be highlighted even more clearly by comparing the predicted mode shapes, as displayed in Fig. 8. As may be observed, it is virtually impossible to distinguish between the FE results and semi-analytical results for the first two modes both in the in-line and in the cross-flow direction. The third mode has been omitted from the figure for the sake of clarity.

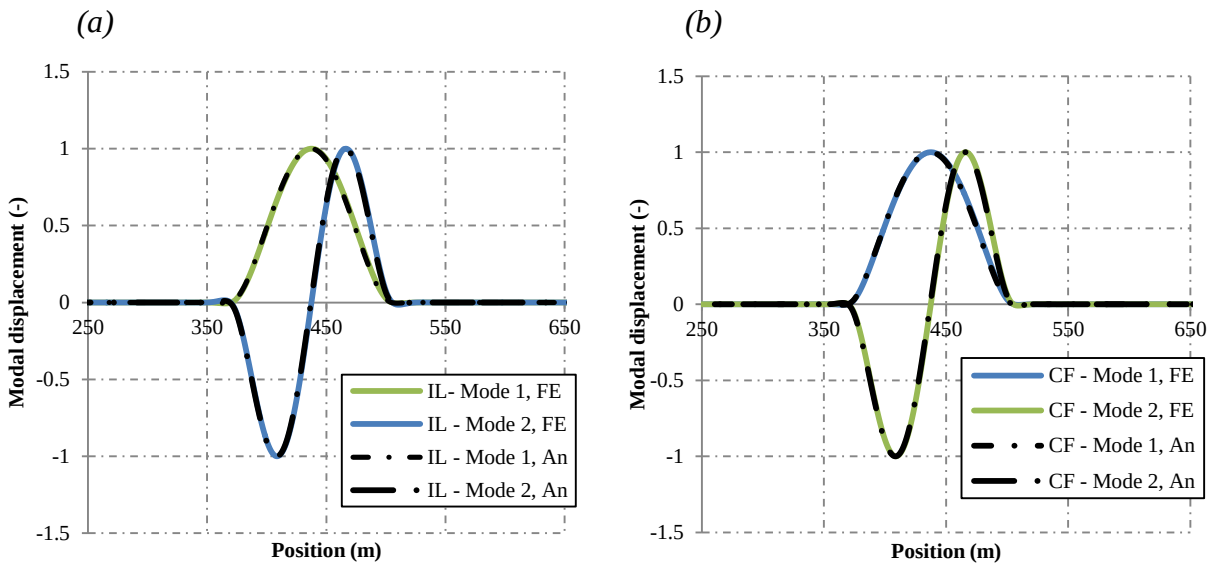

Figure 8 – Mode shapes for *(a)* the first two in-line and *(b)* the first two cross-flow modes for verification case 1 calculated by FE analyses and the semi-analytical ("An") method.

The mode shapes for the in-line modes calculated semi-analytically and by FE are very similar for verification case 16 as well, as can be seen from Fig. 9. The mode shape associated with the lowest frequency has shifted from the first symmetric to the first anti-symmetric mode, whereas the mode shape of the second lowest frequency is associated with a mode

slightly dissimilar to the first symmetric mode. The straight section in the middle of the peak/top of the first symmetric mode, as seen in Fig. 9 (*b*), is caused by the high level of axial tension occurring in the pipe due to large static deflections in this case.

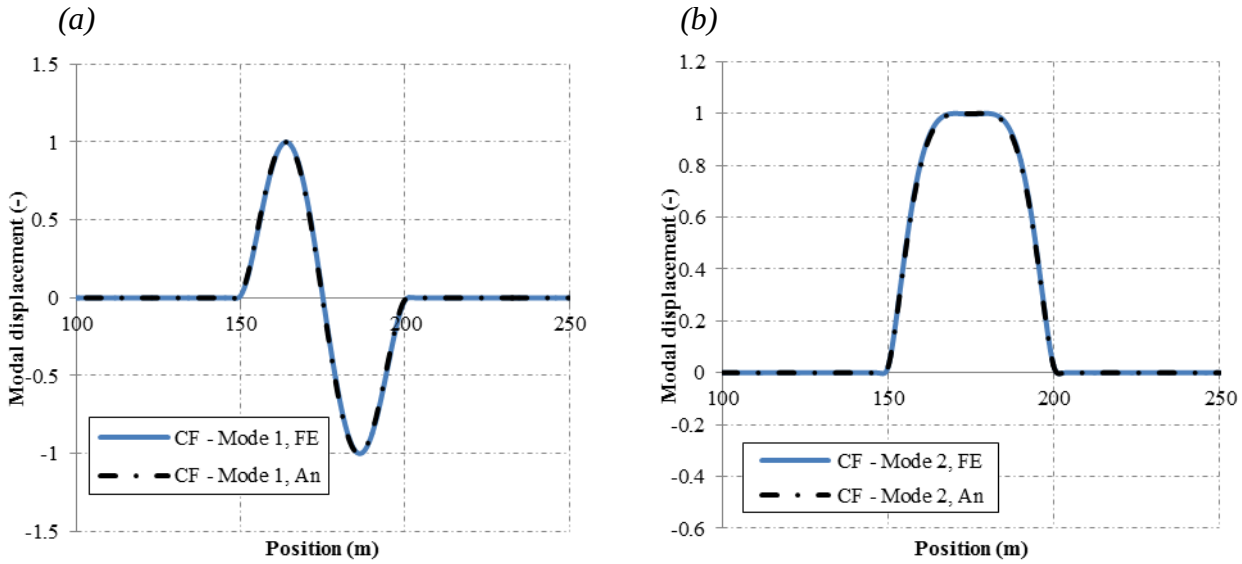

Figure 9 - Mode shapes for *(a)* the cross-flow mode and *(b)* the second cross-flow mode for verification case 16 calculated by FE analyses and the semi-analytical ("An") method.

From the results of the 18 verification cases, we observe that the relative differences between the FE solution and the analytical solution are negligible, with magnitudes of less than 1%, for typical free span configurations like that of verification case 1. For more extreme configurations, as illustrated by verification case 16, the relative differences are also small. Out of 256 compared parameter values, the biggest relative difference is 5.8%, for the second mode cross-flow modal stress for verification case 18. It is important to note that these comments on differences are limited to second or third mode stresses. Fundamental frequencies and stresses are predicted with very high accuracy for all cases studied. Thus, it is clear that the proposed model can be used with confidence for the wide range of parameters investigated.

An interesting observation is that the semi-analytical model developed in this paper is based on Euler-Bernoulli beam theory whereas the shear deformable PIPE31 elements used in the FE analyses are based on Kirchhoff beam theory. Consequently, it has been demonstrated that the effects of shear deformation are negligible for pipeline free span static and dynamic response behavior. This was to be expected considering the slenderness of the pipeline

structures. It should be noted, however, that for a few of the span configurations (verification cases 5-8) a pure shear mode with a frequency close to that of the third in-line mode, was identified in the FE analyses. The shear modes were generally associated with much smaller unit amplitude stresses than the bending modes. In DNV recommended practices, shear dominated response modes are disregarded in terms of VIV, [DNV-RP-F105 2006, DNV-RP-F204, 2010]. The findings from the systematic FE-analyses documented in this report indicate that higher order modes may in some cases be shear dominated. In terms of fatigue damage exposure, shear dominated modes are different from bending dominated modes since shear stresses are parallel to typical weld defects for pipe girth welds whereas bending stresses are perpendicular to typical weld defects. Consequently the fatigue damage is significantly reduced for shear dominated modes compared to bending dominated modes, DNV-RP-C203 [2010]. Considering extreme environmental loading however, stresses induced from shear dominated modes may be as critical as stresses induced from bending dominated modes in terms of typical yield criteria. On the other hand, the current capacity equation in the world leading offshore pipeline design code DNV-OS-F101 [2012] only considers bending moments and axial forces, disregarding shear entirely. Consequently, there would be no practical implication of shear dominated modes in present pipeline design on ultimate limit state considerations. To which extent it is likely to encounter shear dominated modes and to what extent they are critical in typical pipeline design contexts is interesting, and may be subjects of future work.

The computational time, in terms of the CPU seconds, are shown in Table 2 and in Appendix C for each of the analyses by the FE method and the semi-analytical model. The ratios between these times, also shown in the tables, are indicators of the relative computational efficiency of the semi-analytical model as compared to an FE analysis. For standard cases, for which the simple iterative approach given in Fig. 7 yields sufficient accuracy, it is observed that the computational efficiency of the semi-analytical model is on average about 500-600 times faster than the corresponding FE models. For extreme cases where load incrementation is necessary, the difference in computational efficiency is less pronounced, but still with the semi-analytical method performing 10-20 times faster than standard finite element analysis.

6.2 Comparisons with the Semi-Empirical Model of Fyrileiv and Mørk

In the previous section and in Appendix C, it has been demonstrated that predictions by the proposed semi-analytical model are negligibly different from those of detailed FE analyses, regardless of level of effective axial force, relative span length and magnitude of vertical static displacements. Consequently, results of the semi-analytical model are sufficiently accurate to be considered exact for the purpose of evaluating the approach by Fyrileiv and Mørk [2002]. Below, results will be presented that document the impact of having a more accurate semi-analytical solution compared to the existing semi-empirical solution of Fyrileiv and Mørk. Parametric studies have been undertaken in order to document the effects of relative span length, level of effective axial force and magnitude of static deflection on the accuracy of the analytical formulae of Fyrileiv and Mørk for frequencies and modal stresses both inside and outside their range of applicability. It is, however, important to note that the frequencies, stresses and static deflections depend on more parameters than the ones investigated. The static and dynamic soil stiffnesses, the bending stiffness and axial stiffness, and the effective mass also influence the results, implying that the results presented in this section are not general, but valid for the given set of configurations. Changing the static and dynamic soil stiffnesses, the bending to axial stiffness ratio or the effective mass, or a combination of the three, will result in different variations between the semi-empirical method of Fyrileiv and Mørk compared to the semi-analytical model developed in this paper.

In operation, pipelines are generally in axial compression, see Eq. (1), but in temporary and shut-down conditions, pipelines are generally in axial tension. Cases with compressive axial force become unrealistic for relative lengths over 160-200, depending on weight and bending stiffness, since the static deflections become excessive. Taking pipeline data from verification case 6, see Tables C.1-C.3 (Appendix C), the relative free span length was varied in the range between 50 to 225. In order to study such long spans with some degree of realism, an example with high axial tension was chosen.

In Fig. 10, the fundamental in-line and cross-flow frequencies are shown for the semi-analytical solution developed in this paper alongside with corresponding results from the semi-empirical solutions of Fyrileiv and Mørk.

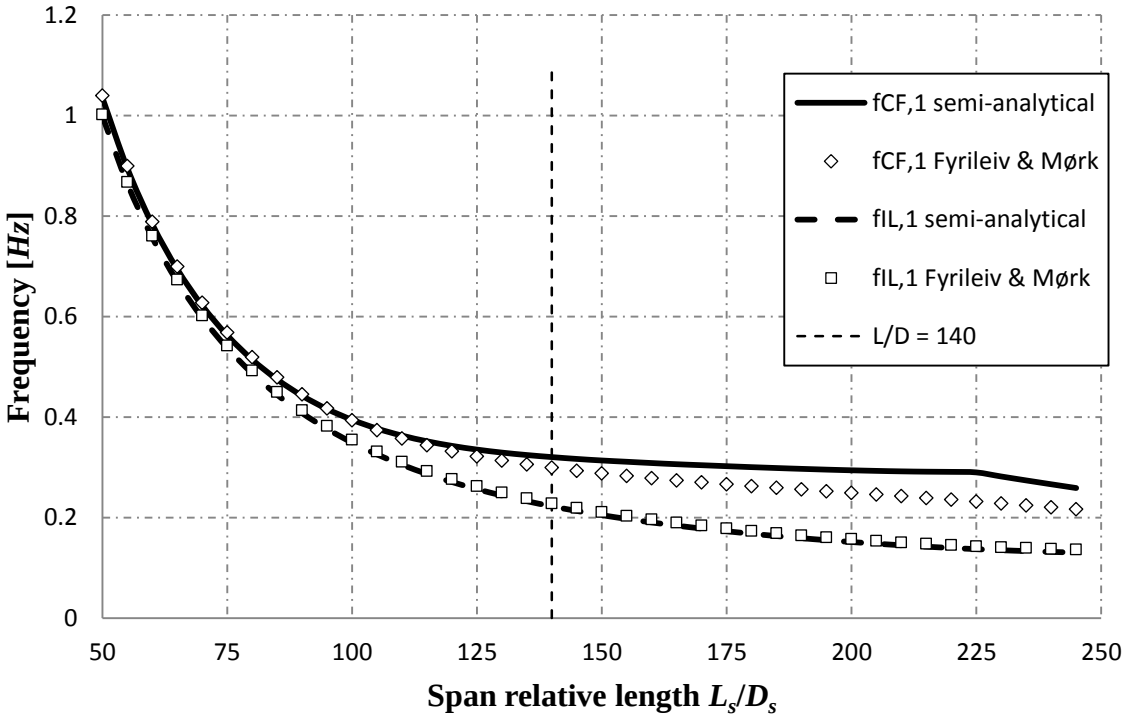

Figure 10 – Comparison of fundamental in-line and cross-flow frequencies as a function of relative span length, calculated with the semi-analytical method and with the method of Fyrileiv and Mørk.

For the in-line frequencies, shown in Fig.10 by the dashed line for the semi-analytical method and open squares for the semi-empirical method, it can be observed that they almost coincide over the full range of the comparisons. For the in-line direction, the biggest relative difference between the semi-analytical and semi-empirical methods is 4.6%, with relative differences increasing for increasing L_s/D_s. Consequently, the semi-empirical model gives excellent predictions for in-line fundamental frequencies also for $L_s/D_s > 140$ in the present example.

However, the cross-flow frequencies do not compare equally well. For $L_s/D_s < 100$, the semi-empirical model, shown by open diamonds, predicts frequencies accurately, but for increasing L_s/D_s ratios it underestimates frequencies. The largest relative difference between the models is 24.9%, but limited to 7.1% if $L_s/D_s < 140$. There are two reasons why the cross-flow frequency is less accurately predicted by the semi-empirical method than the in-line frequency. First, the sag term in Eq. (44) is not dependent on the axial stiffness of the pipe, whereas in Eq. (37) it is demonstrated that the axial stiffness contributes to the influence of the static deformation configuration on the cross-flow modal response. Second, for large vertical static deflections, the stiffening effect introduced by the static deformation

configuration suppresses the first symmetric cross-flow mode, and the first anti-symmetric mode gives the lower frequency. This is not reflected in the semi-empirical approach (Eq. (44)), and explains why the semi-empirical method underestimates the frequency for pipes with significant static deflections, associated with large span lengths. For instance, for the relative length of 225 in the figure, the static mid-span deflection is as high as 5D. The same effect is found for verification case 16, as shown previously in Fig. 9. The fact that Eq. (44) does not account for a potential change in mode shape, is one of the main reasons for the limitation in range of applicability in terms of δ/D for the semi-empirical model [DNV-RP-F105, 2006].

The modal stresses associated with the cases shown in Fig. 10 are compared in Fig. 11. Comparing Eqs. (40) and (48) the maximum relative differences (relative to the results of the semi-analytical model, which is considered to be the most accurate) for unit diameter in-line and cross-flow stress amplitudes, disregarding $L_s/D_s > 225$ cross-flow, is 43% in-line and 50.7% cross-flow. If $L_s/D_s < 140$, these relative differences decrease to 5.4% in-line and 14.7% cross-flow. Consequently, the semi-empirical model by Fyrileiv and Mørk is more accurate for estimating frequencies than for estimating modal stresses.

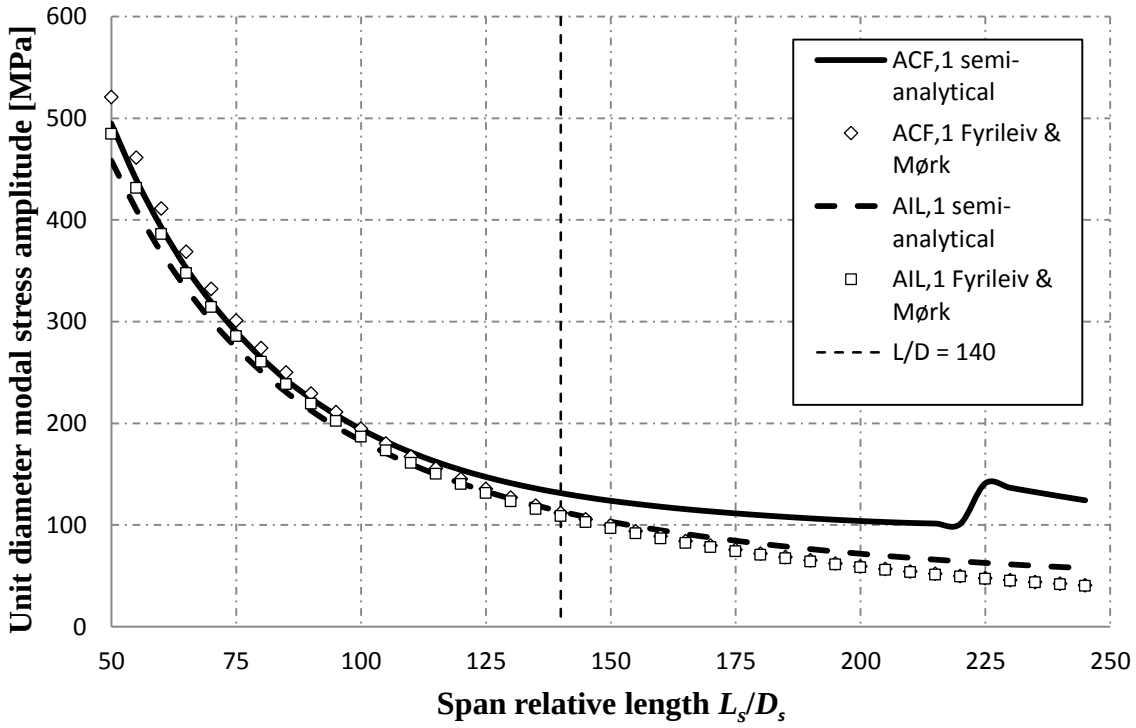

Figure 11 – Modal stresses for the cases shown in Fig. 10 calculated with the semi-analytical method and with the method of Fyrileiv and Mørk.

In Eq. (48) there is little distinction between the in-line and the cross-flow modal stress. The only difference is the effective length, which relates to the differences in in-line versus cross-flow dynamic soil stiffness. Consequently, if the in-line and cross-flow dynamic soil stiffnesses were equal, Eq. (48) would yield the same result for in-line and cross-flow modal stress. As the span length increases, the overall bending resistance decreases significantly whereas the soil stiffness remains the same. Consequently, the soil stiffness relative to the bending stiffness increases along with the span length. The results of this can be observed from Fig. 11. Since the boundary condition becomes increasingly stiff, converging towards a fixed-fixed configuration, it may be observed that as the length increases, the curves representing modal stresses predicted by Eq. (48) fall onto one another for in-line and cross-flow modal stresses, as seen in Fig. 11. There is, however, a different behavior to observe from the in-line and cross-flow modal stresses predicted by the semi-analytical model. As the free span length increases, the difference between in-line and cross-flow modal stress increases as well. An intuitive explanation for this phenomenon may be found by

understanding the stiffening effect of the static deflection on the cross-flow modal response. As the span length increases, so do the static deflections. When the static deflections increase, the increased stiffness causes subsequent increases in the modal stresses. Additionally, for the relative length 225, a change of slope in the curve for fundamental cross-flow frequency was observed in Fig. 10. Similarly, a jump in the curve is observed for the cross-flow modal stress in Fig. 11, for the relative length 225. The change in mode shape from the first symmetric mode to the first anti-symmetric mode, which has steeper curvatures, necessarily results in higher associated modal stresses.

In Fig. 12 the same pipe as given in the verification case 6 is used, but the free span length is kept constant at 75 metres and the effective axial force is varied between ± 0.60 P_{cr}, where P_{cr} is calculated according to Eq. (47).

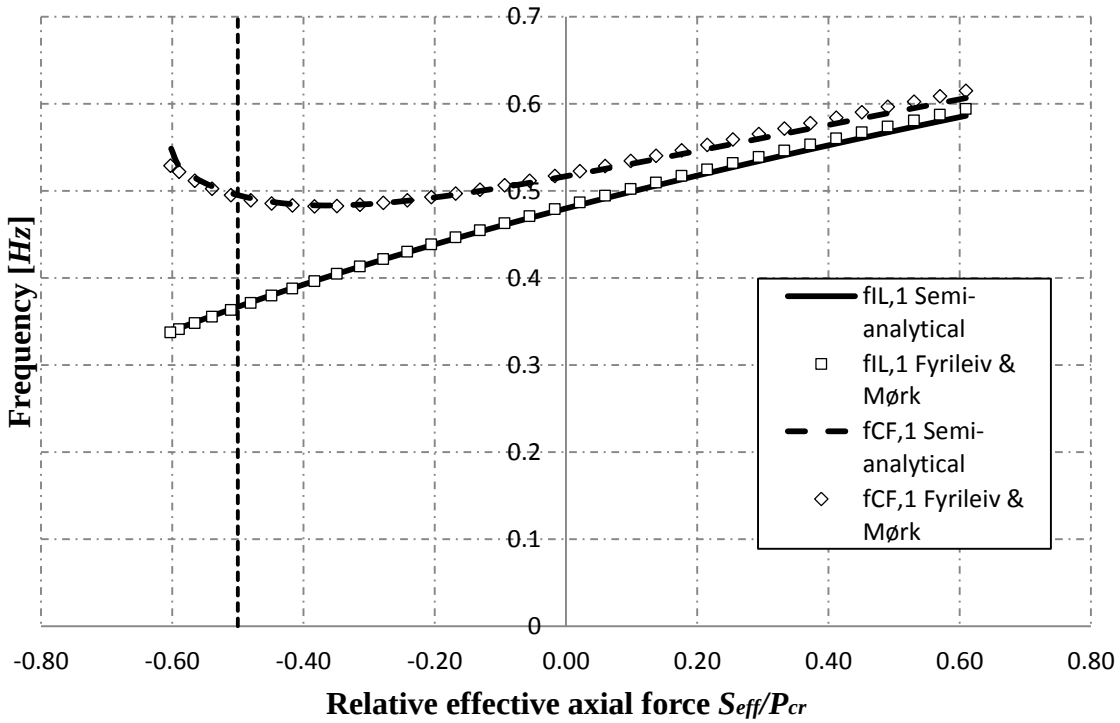

Figure 12 – Fundamental frequencies as a function of relative axial force calculated with both the semi-analytical method and the method of Fyrileiv and Mørk. The relative span length is the same for all cases.

From Fig. 12 it can be observed that the in-line frequencies estimated by the semi-analytical model and the semi-empirical model follow the same trend and agree very well. The biggest

relative difference between the fundamental in-line frequencies from the two methods is 1.3%, a percentage which does not vary particularly with the magnitude of effective axial force. The semi-empirical model systematically overestimates the fundamental cross-flow frequency, albeit with a modest relative difference peaking at 1.7% when confined to the range of applicability of the semi-empirical model. Outside this range, the relative difference grows to 4.0% for $P_{cr} = -0.6$. The differences between the calculation results for the in-line and cross-flow frequencies are due to the sag term in Eq. (44) for the semi-empirical method and the axial coupling due to out of straightness for the semi-analytical model.

The modal stress amplitudes corresponding to the frequencies presented in Fig. 12 are given in Fig. 13.

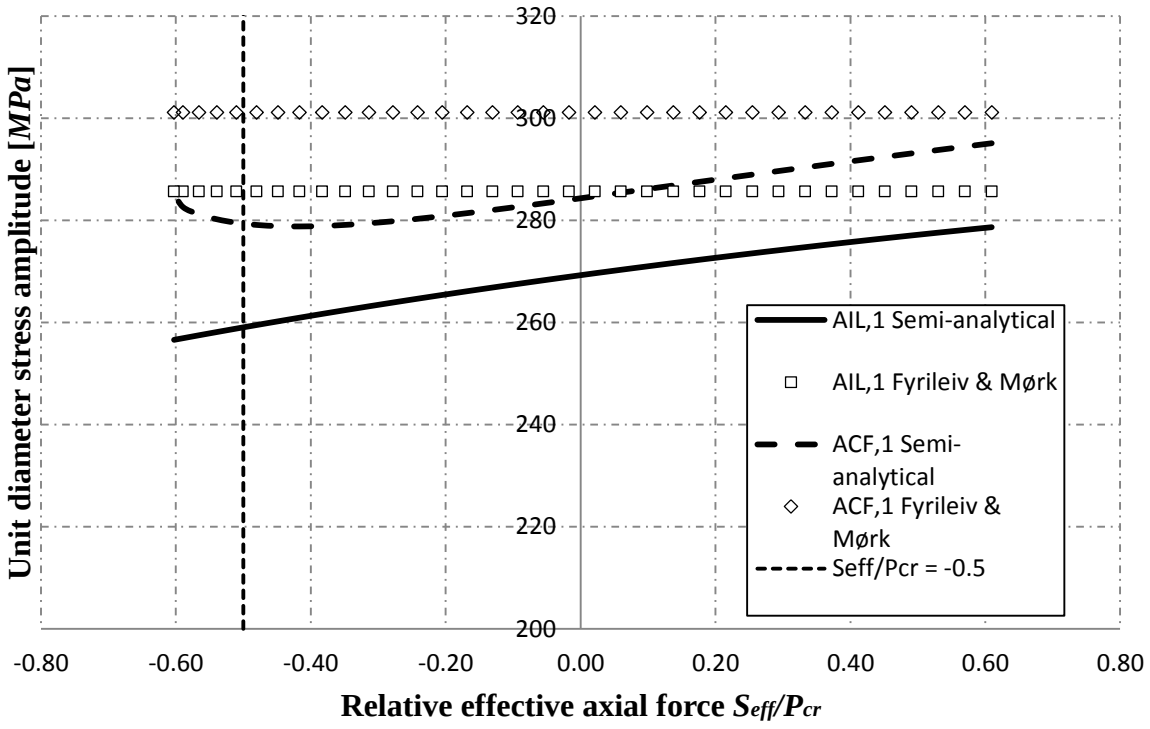

Figure 13 – Modal stresses for the cases shown in Fig. 12 calculated with the semi-analytical method and with the method of Fyrileiv and Mørk.

It can be observed from the semi-empirical method's Eq. (48) that the unit diameter stress amplitude does not depend on the effective axial force. However, when increasing the effective axial force, i.e. by adding tension, the resistance against bending deformation

increases. The stresses in the pipeline are proportional to the stiffness and to the displacements. Since the maximum displacement here is normalized to a unit diameter, the increased geometric stiffness of pipes in tension causes increased stresses. Consequently, an increase in modal stresses with applied tension might be expected, as observed for the semi-analytical model in Fig. 13. Note that the significant stiffening effect due to large static deflections at $S_{eff} < -0.5\ P_{cr}$ causes increased cross-flow stresses. The peak relative differences between the two models are 10.2% in-line and 8.4% cross-flow.

7 CONCLUSIONS

- A semi-analytical model for the dynamics analysis of pipelines with free spans have been developed, and comparisons have been made with FE analyses and the semi-empirical approach developed by Fyrileiv and Mørk (and adopted by DNV in their recommendations [DNV-RP-F105, 2006]).
- The semi-analytical model is accurate to within 1% deviation compared to detailed FE analyses, for most relevant response quantities. For calculations of stresses associated with higher order modes, the deviations from FE solutions may sometimes reach up to 5-6%.
- Euler-Bernoulli beam theory is sufficient with regard to pipeline free span modeling, since shear deformation has been shown not to influence the static and dynamic response behavior.
- The semi-analytical model is 500-600 times faster than typical detailed FE analyses with no loss of accuracy for typical span configurations. For extreme span lengths the semi-analytical model is 10-20 times faster than detailed FE analyses.
- Compared to the semi-empirical method developed by Fyrileiv and Mørk, the semi-analytical model has better accuracy, particularly for modal stresses, and no practical limitations on range of validity with respect to relative span length and mid-span deflection.

ACKNOWLEDGEMENTS

The authors would like to extend their gratitude to Professor Jostein Hellesland at the University of Oslo for excellent discussions and revisions of the text, Dr.Philos. Olav Fyrileiv, Senior Principal Engineer at DNV, for good comments on physical aspects and experience with free spans and free span design, and finally to Dr.Psychol. Elisabeth Backe-Hansen for excellent review of the text itself.

REFERENCES

ABAQUS, v. 6.12, Dassault Systèmes Simulia Corp., Providence, RI, USA, 2012

Axisa, F. and Trompette, P. "Modelling of Mechanical Systems: Structural Elements, Volume 2", Butterworth-Heinemann, 2005, ISBN 0750668466

Blevins, R.D. "Flow-induced vibrations", Krieger, 1997, ISBN 0442206518

Brubak, L., Hellesland, J. and Steen, E. "Semi-analytical buckling strength analysis of plates with arbitrary stiffener arrangements", 2007, Journal of Constructional Steel Research, 63, pp. 532–543

Brubak, L. and Hellesland, J. "Approximate buckling strength analysis of arbitrarily stiffened, stepped plates", 2007a, Engineering Structures, 29, pp. 2321–2333

Brubak, L. and Hellesland, J. "Semi-analytical postbuckling and strength analysis of arbitrarily stiffened plates in local and global bending", 2007b, Thin-Walled Structures, 45, pp. 620-633

Brubak, L. and Hellesland, J. "Strength criteria in semi-analytical, large deflection analysis of stiffened plates in local and global bending", 2008, Thin-Walled Structures, 46, pp. 1382-1390

Bruschi, R. and Vitali, L. "Large-amplitude oscillations of geometrically non-linear elastic beams subjected to hydrodynamic excitation", 1991, Journal of offshore mechanics and arctic engineering, 113(2), pp. 92-104

Charpie, J.P. "An analytical model for the free in-plane vibration of beams of variable curvature and thickness", 1991, Ph.D. thesis, The Pennsylvania State University

Charpie, J.P. and Burroughs, C.B. "An analytical model for the free in-plane vibration of beams of variable curvature and depth", 1993, Journal of the Acoustical Society of America, 94(2), pp. 866-879

Choi, H.S. "Free spanning analysis of offshore pipelines", Ocean Engineering, 2001, 28, pp. 1325-1338

Cook R.D., Malkus D.S, Plesha M. E. and Witt R. J., "Concepts and applications of finite element analysis", Wiley, 4th ed., 2002, ISBN: 0-471-35605-0

DNV-OS-F101. "Submarine Pipeline Systems", Det Norske Veritas, August 2012.

DNV-RP-C205, "Environmental Loads and Environmental Conditions", Det Norske Veritas, Oct. 2010

DNV-RP-C203, "Fatigue of offshore steel structures", Det Norske Veritas, April 2010.

DNV-RP-F105, "Free Spanning Pipelines", Det Norske Veritas, Feb. 2006

DNV-RP-F110, "Global Buckling of Submarine Pipelines", Det Norske Veritas, Oct. 2007

DNV-RP-F203, “Riser Fatigue”, Det Norske Veritas, Oct. 2010

FatFree, “Fatigue of Free Spanning Pipelines”, v.10.6, Det Norske Veritas, Norway, DNV Report No. 2000-3283, 2007

Fyrileiv, O. and Collberg, L. “Influence of pressure in pipeline design – effective axial force”, Proc. of 24th int. conf. on offshore mechanics and arctic engineering, OMAE 2005, Halkidiki, Greece, June 12-17

Fyrileiv, O. and Mørk, K. “Structural response of pipeline free spans based on beam theory”, Proc. of 21st int. conf. on offshore mechanics and arctic engineering, OMAE 2002, Oslo, Norway, June 23-28, 2002

Fyrileiv, O., Mørk, K.J. and Rongved, K. “Togi pipeline – assessment of non-stationary free spans”, Proc. of 19th int. conf. on offshore mechanics and arctic engineering, OMAE 2000, New Orleans, LA, Feb. 14-17

Fyrileiv, O., Mørk, K.J. and Chezhian, M. “Experiences using DNV-RP-F105 in assessment of free spanning pipelines”, Proc. of 24th int. conf. on offshore mechanics and arctic engineering, OMAE 2005, Halkidiki, Greece, June 12-17

Fyrileiv, O., Mørk, K.J., Kathrud, K. and Sortland, L. “Free span assessment of the Zeepipe IIA Pipeline”, Proc. of 17th int. conf. on offshore mechanics and arctic engineering, OMAE 1998, Lisbon, July 6-9

Hagen, Ø., Mørk, K.J., Verley, R., Sortland L. and Nes, H. “Evaluation of free spanning design in a risk based perspective”, Proc. of 22nd int. conf. on offshore mechanics and arctic engineering, OMAE 2003, Cancun, Mexico, June 8-13

Hobbs, R.E. “Influence of structural boundary conditions on pipeline free span dynamics”, Proc. of 5th int. conf. on offshore mechanics and arctic engineering, OMAE 1986, Tokyo

Kirkhope, J. “In-plane vibrations of a thick circular ring”, Journal of Sound and Vibration, 1977, 50, pp. 219-227

MATLAB version 7.11.2010b. Natick, Massachusetts: The MathWorks Inc., 2010

Mørk, K.J., Fyrileiv, O., Chezhian, M., Nielsen, F.G. and Søreide, T. “Assessment of VIV induced fatigue in long free spanning pipelines”, Proc. of 22nd int. conf. on offshore mechanics and arctic engineering. OMAE 2003, Cancun, Mexico, June 8-13

Netenhyi, M. “Beams on elastic foundations: Theory with applications in the fields of civil and mechanical engineering”, University of Michigan press, 1946, ISBN-10: 0472084453

Shames, I.H. and Dym, C.L. “Energy and Finite Element Methods in Structural Mechanics: SI Units Edition”, Taylor & Francis Group, 2nd ed., 1991, ISBN 0891169423

Sparks, C.P., “The Influence of Tension, Pressure and Weight on Pipe and Riser Deformations and Stresses”, Transactions of the ASME, 1984, 106, pp. 46-54

Srivastava, A.K. and Gope, P.C. “Strength of Materials”, Prentice-Hall of India Pvt. Ltd., 2007, ISBN-10 8120332741

Steen E, Byklum E, Hellesland J. “Elastic postbuckling stiffness of biaxially compressed rectangular plates.” Engineering Structures, 2008; 30(10), pp. 2631-2643

Steen, E., Byklum, E., Vilming, K.G. and Østvold, T.K., "Computerized buckling models for ultimate strength assessments of stiffened ship hull panels", Proceedings of The Ninth International Symposium on Practical Design of Ships and other Floating Structures, Lübeck-Travemünde, Germany, 2004, pp. 235-242

Steen E, Byklum E. "Ultimate strength and postbuckling stiffness of plate panels subjected to combined loads using semi-analytical models." In: Proceedings, international conference on marine research and transportation, 2005

Sumer, B.M. and Fredsøe, J. "Hydrodynamics around cylindrical structures", Adv. Series on Ocean Eng., Vol. 12, World Scientific, 2006, ISBN 9812700390

Tarnopolskaya, T., De Hoog, F., Fletcher, N.H. and Thwaites, S. "Asymptotic analysis of the free in-plane vibrations of beams with arbitrarily varying curvature and cross-section", Journal of Sound and Vibration, 1996, Vol. 196, pp. 659-680

Timoshenko, S. "Strenght of materials part I and II", Krieger publishing company, 3rd ed., 1983, ISBN-10: 0898746213

Wu, J.S. "In-plane vibration of extensional curved non-uniform beams", 2009, PhD thesis, Dept. of Mech. Eng., National Cheng Kung University, Tainan, Taiwan

APPENDIX A

In this appendix, explicit expressions for Eq. (31) will be deduced. For ease of reference, Eq. (37) is restated:

$$\begin{aligned}
\mathbf{K}_{11} &= EA\int_0^L \mathbf{N}_{u,s}^T \mathbf{N}_{u,s}\, ds \\
\mathbf{K}_{12} &= -EA\int_0^L \kappa \mathbf{N}_{u,s}^T \mathbf{N}_{v}\, ds \\
\mathbf{K}_{22} &= EA\int_0^L \kappa^2 \mathbf{N}_{v}^T \mathbf{N}_{v}\, ds + EI\int_0^L \mathbf{N}_{v,ss}^T \mathbf{N}_{v,ss}\, ds \\
\mathbf{K}_{21} &= \mathbf{K}_{12}^T
\end{aligned} \tag{A.1}$$

$\mathbf{K}_{11}$ is given in Eq. (30). The remaining two matrices to determine are $\mathbf{K}_{12}$ and $\mathbf{K}_{22}$. Matrix $\mathbf{K}_{12}$ will be developed first after which $\mathbf{K}_{22}$ is developed in this appendix. If inserted for the static curvature κ, Eq. (38), and $\mathbf{N}$, given in Eq. (16), an expression for $\mathbf{K}_{12}$ can be found:

$$\left(\mathbf{K}_{12}\right)_{ij} = EAi\left(\frac{\pi}{L}\right)^3 \int_0^L \cos\left(\frac{i\pi s}{L}\right)\sin\left(\frac{j\pi s}{L}\right)\sum_{a=1}^{n} a^2 D_{static,a} \sin\left(\frac{a\pi s}{L}\right) ds \tag{A.2}$$

This requires integrals on the form:

$$I_{12} = \int_0^L \cos\left(\frac{i\pi s}{L}\right)\sin\left(\frac{j\pi s}{L}\right)\sin\left(\frac{a\pi s}{L}\right) ds \tag{A.3}$$

Using two trigonometric identities transforms the integrals to the form:

$$\begin{aligned}
I_{12} = \frac{1}{4}\Bigg[&\int_0^L \cos\left(\frac{\pi s}{L}\left(i+j-a\right)\right) ds - \int_0^L \cos\left(\frac{\pi s}{L}\left(i+j+a\right)\right) ds \\
&- \int_0^L \cos\left(\frac{\pi s}{L}\left(i-j-a\right)\right) ds + \int_0^L \cos\left(\frac{\pi s}{L}\left(i-j+a\right)\right) ds \Bigg]
\end{aligned} \tag{A.4}$$

Inserting for Eq. (A.4) into Eq. (A.2) gives:

$$\begin{aligned}
\left(\mathbf{K}_{12}\right)_{ij} = \frac{EAi}{4}\left(\frac{\pi}{L}\right)^3 \int_0^L \sum_{a=1}^{n} a^2 D_{static,a} \Bigg[&\cos\left(\frac{\pi s}{L}\left(i+j-a\right)\right) - \cos\left(\frac{\pi s}{L}\left(i+j+a\right)\right) \\
&- \cos\left(\frac{\pi s}{L}\left(i-j-a\right)\right) + \cos\left(\frac{\pi s}{L}\left(i-j+a\right)\right) \Bigg] ds
\end{aligned} \tag{A.5}$$

In Eq. (A.4), each integral over cosines are either L, if the argument is zero, or zero if the combination of i, j and a is nonzero, since i, j and a are integers. The second cosine term, with argument a factor of $i + j + a$, is never zero since i, j and a are strictly positive. Consequently, the expression for $\mathbf{K}_{12}$ can be given explicitly:

$$\left(\mathbf{K}_{12}\right)_{ij} = \frac{EA}{4}\left(\frac{\pi}{L}\right)^3 i\sum_{a=1}^{n} a^2 D_{static,a}\left(k_{12}^1 + k_{12}^2 + k_{12}^3\right) \tag{A.6}$$

Where:

$$\begin{aligned} k_{12}^1 &= \begin{cases} L, & i+j-a=0 \\ 0, & i+j-a\neq 0 \end{cases} \\ k_{12}^2 &= \begin{cases} -L, & i-j-a=0 \\ 0, & i-j-a\neq 0 \end{cases} \\ k_{12}^3 &= \begin{cases} L, & i-j+a=0 \\ 0, & i-j+a\neq 0 \end{cases} \end{aligned} \tag{A.7}$$

The establishment of $\mathbf{K}_{12}$ does however include summation over a for each individual i. If $\mathbf{K}_{12}$ is established by performing the tests in Eq. (A.7) for every combination of i, j and a, the generation of $\mathbf{K}_{12}$ is performed to the order of $O(n^3)$. This is slower than the eigenvalue solution, so it is desirable to achieve a faster solution to Eq. (A.6). The calculation efficiency for $\mathbf{K}_{12}$ can fortunately be improved significantly, all the way to $O(n)$, since direct calculation of the sums in Eq.(A.6) are possible.

$k_{12}{}^1$ is defined by Eqs. (A.6) and (A.7). The equation $i + j - a = 0$ can be solved to yield $a = i + j$. It is desirable to transform the idea of $k_{12}{}^q$, $q \in \{1, \quad 2, \quad 3\}$, to matrix expressions which incorporate the whole sum in Eq. (A.6), such that $\mathbf{K}_{12}$ can be determined based on sums of matrices:

$$\begin{aligned} \left(\mathbf{k}_{12}^1\right)_{ij} &= \sum_{a=1}^{n} a^2 D_{static,a} k_{12}^1 \\ \left(\mathbf{k}_{12}^2\right)_{ij} &= \sum_{a=1}^{n} a^2 D_{static,a} k_{12}^2 \\ \left(\mathbf{k}_{12}^3\right)_{ij} &= \sum_{a=1}^{n} a^2 D_{static,a} k_{12}^3 \end{aligned} \tag{A.8}$$

By combining Eqs. (A.6) and (A.8), a matrix summation can be developed for Eq. (A.6):

$$\left(\mathbf{K}_{12}\right)_{ij} = \frac{EA}{4}\left(\frac{\pi}{L}\right)^3 i\left(\mathbf{k}_{12}^1 + \mathbf{k}_{12}^2 + \mathbf{k}_{12}^3\right)_{ij} \tag{A.9}$$

Next, $\mathbf{k}_{12}{}^1$ is established. If organized in a matrix, the position and value of $i+j$ is:

$$\begin{bmatrix} 2 & 3 & 4 & 5 & \cdots & n+1 \\ 3 & 4 & 5 & \vdots & \cdots & n+2 \\ 4 & 5 & \vdots & \vdots & \cdots & n+3 \\ 5 & \vdots & \vdots & \ddots & \cdots & n+4 \\ \vdots & \vdots & \vdots & \vdots & \ddots & \vdots \\ n+1 & n+2 & n+3 & n+4 & \cdots & 2n \end{bmatrix} \tag{A.10}$$

In Eq. (A.10), along lines perpendicular to the diagonal, $i + j$ has constant values:

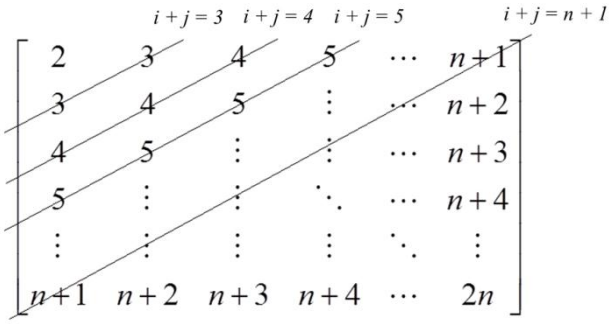

Figure 14 – Illustration of banded structure for the matrix containing the values of the sums of its indices.

Along the lines where $i + j$ are constant, only one value of a yields $i + j - a = 0$. Furthermore, a is bounded by:

$$a \in \{1, \quad 2, \quad \ldots \quad n\} \tag{A.11}$$

Consequently $\mathbf{k}_{12}{}^1$ only has entries where $i + j < n + 1$. Inserting for Eq. (A.8), gives the following expression for $\mathbf{k}_{12}{}^1$:

$$\mathbf{k}_{12}^1 = L\begin{bmatrix} 2^2 D_{static,2} & 3^2 D_{static,3} & 4^2 D_{static,4} & \cdots & n^2 D_{static,n} & 0 \\ 3^2 D_{static,3} & 4^2 D_{static,4} & \vdots & n^2 D_{static,n} & 0 & \\ 4^2 D_{static,4} & \vdots & n^2 D_{static,n} & 0 & & \\ \vdots & n^2 D_{static,n} & 0 & & & \\ n^2 D_{static,n} & 0 & & & \mathbf{0} & \\ 0 & & & & & \end{bmatrix} \tag{A.12}$$

With a similar methodology, expressions for $\mathbf{k}_{12}{}^2$ and $\mathbf{k}_{12}{}^3$ can be determined:

$$\mathbf{k}_{12}^{2} = -L\begin{bmatrix} 0 & & & & & \\ D_{static,1} & 0 & & & & \mathbf{0} \\ 2^2 D_{static,2} & D_{static,1} & 0 & & & \\ \vdots & 2^2 D_{static,2} & D_{static,1} & \ddots & & \\ (n-2)^2 D_{static,n-2} & \vdots & \ddots & \ddots & \ddots & \\ (n-1)^2 D_{static,n-1} & (n-2)^2 D_{static,n-2} & \vdots & 2^2 D_{static,2} & D_{static,1} & 0 \end{bmatrix}$$

$$\mathbf{k}_{12}^{3} = L\begin{bmatrix} 0 & D_{static,1} & 2^2 D_{static,2} & \cdots & (n-2)^2 D_{static,n-2} & (n-1)^2 D_{static,n-1} \\ & 0 & D_{static,1} & 2^2 D_{static,2} & \vdots & (n-2)^2 D_{static,n-2} \\ & & 0 & D_{static,1} & \ddots & \vdots \\ & & & \ddots & \ddots & 2^2 D_{static,2} \\ & \mathbf{0} & & & \ddots & D_{static,1} \\ & & & & & 0 \end{bmatrix} \quad \textbf{(A.13)}$$

Having established expressions for $\mathbf{K}_{11}$ and $\mathbf{K}_{12}$ it remains to determine an explicit expression for $\mathbf{K}_{22}$:

$$\mathbf{K}_{22} = EA\int_0^L \kappa_s{}^2 \mathbf{N}_v^T \mathbf{N}_v ds + EI\int_0^L \mathbf{N}_{v,ss}^T \mathbf{N}_{v,ss} ds \quad \textbf{(A.14)}$$

The bending stiffness term in Eq. (A.14) is presented in Eq. (30) and will not be repeated here. The axial stiffness term is found by first inserting for the static curvature:

$$(\mathbf{K}_{22})_{ij} = EA\left(\frac{\pi}{L}\right)^4 \int_0^L \sin\left(\frac{i\pi s}{L}\right)\sin\left(\frac{j\pi s}{L}\right)\sum_{b=1}^{n}\sum_{a=1}^{n} a^2 b^2 D_{static,a} D_{static,b} \sin\left(\frac{a\pi s}{L}\right)\sin\left(\frac{b\pi s}{L}\right) ds + EI\frac{(i\pi)^4}{2L^3}\delta_{ij} \quad \textbf{(A.15)}$$

where δ_{ij} is the Kroenecker delta. The above integral includes integrations on the form:

$$I_{22} = \int_0^L \sin\left(\frac{i\pi s}{L}\right)\sin\left(\frac{j\pi s}{L}\right)\sin\left(\frac{a\pi s}{L}\right)\sin\left(\frac{b\pi s}{L}\right) ds \quad \textbf{(A.16)}$$

Again applying trigonometric identities, the integral Eq. (A.16) can be transformed:

$$I_{22}=\frac{1}{8}\left[\int_0^L\cos\left(\frac{(i-j-a+b)\pi s}{L}\right)ds+\int_0^L\cos\left(\frac{(i-j+a-b)\pi s}{L}\right)ds+\int_0^L\cos\left(\frac{(i-j-a-b)\pi s}{L}\right)ds\right.$$
$$+\int_0^L\cos\left(\frac{(i-j+a+b)\pi s}{L}\right)ds-\int_0^L\cos\left(\frac{(i+j-a+b)\pi s}{L}\right)ds-\int_0^L\cos\left(\frac{(i+j+a-b)\pi s}{L}\right)ds \quad \textbf{(A.17)}$$
$$\left.-\int_0^L\cos\left(\frac{(i+j-a-b)\pi s}{L}\right)-\int_0^L\cos\left(\frac{(i+j+a+b)\pi s}{L}\right)ds\right]$$

Since *i*, *j*, *a* and *b* are integers, any nonzero combination of *i*, *j*, *a* and *b* for an individual cosine term results in a zero result for the integral. Consequently, only for combinations of *i*, *j*, *a* and *b* equaling zero provides nonzero results. The last cosine term has argument of $i + j + a + b$ which is nonzero for all relevant *i*, *j*, *a* and *b* and consequently this term is exactly zero and will be disregarded in the following. Following a similar line of thought as for the computation of $\mathbf{K}_{12}$, $\mathbf{K}_{22}$ may be expressed as follows:

$$\left(\mathbf{K}_{22}\right)_{ij}=\frac{EA}{8}\left(\frac{\pi}{L}\right)^4\sum_{a=1}^{n}\sum_{b=1}^{n}a^2b^2D_{static,a}D_{static,b}\left(k_{22}^1+k_{22}^2+k_{22}^3+k_{22}^4+k_{22}^5+k_{22}^6+k_{22}^7\right) \quad \textbf{(A.18)}$$

Comparing Eqs. (A.17) and (A.18) gives:

$$k_{22}^1=\begin{cases}L, & i-j-a+b=0\\ 0, & i-j-a+b\neq 0\end{cases}$$
$$k_{22}^2=\begin{cases}L, & i-j+a-b=0\\ 0, & i-j+a-b\neq 0\end{cases}$$
$$k_{22}^3=\begin{cases}-L, & i-j-a-b=0\\ 0, & i-j-a-b\neq 0\end{cases}$$
$$k_{22}^4=\begin{cases}-L, & i-j+a+b=0\\ 0, & i-j+a+b\neq 0\end{cases} \quad \textbf{(A.19)}$$
$$k_{22}^5=\begin{cases}-L, & i+j-a+b=0\\ 0, & i+j-a+b\neq 0\end{cases}$$
$$k_{22}^6=\begin{cases}-L, & i+j+a-b=0\\ 0, & i+j+a-b\neq 0\end{cases}$$
$$k_{22}^7=\begin{cases}L, & i+j-a-b=0\\ 0, & i+j-a-b\neq 0\end{cases}$$

The establishment of $\mathbf{K}_{22}$ does however include summation over *a* and b for each individual combination of *i* and *j*. If $\mathbf{K}_{22}$ is established by performing the tests in Eq. (A.19) for every combination of *i*, *j*, *a* and b, the generation of $\mathbf{K}_{22}$ is performed to the order of $O(n^4)$ flops, since summations must be performed for each test. $O(n^4)$ is two orders slower than the

eigenvalue solution, so it is important to achieve a faster solution to Eq. (A.18). The calculation efficiency for $\mathbf{K}_{22}$ can fortunately be improved significantly, all the way to $O(n^2)$, by a combinatoric argument. As for the case of Eqs. (A.6) and (A.8), it is desirable to determine matrix expressions for $k_{22}{}^q,\ q \in \{1, \quad \dots \quad 7\}$. By making the following substitution:

$$\left(\mathbf{k}_{22}^{q}\right)_{ij} = \sum_{a=1}^{n}\sum_{b=1}^{n} a^2 b^2 D_{static,a} D_{static,b} k_{22}^{q}, \quad q \in \{1, \quad \dots \quad 7\} \tag{A.20}$$

Eqs. (A.20) and (A.18) can be combined in order to achieve a matrix summation expression for $\mathbf{K}_{22}$:

$$\left(\mathbf{K}_{22}\right)_{ij} = \frac{EA}{8}\left(\frac{\pi}{L}\right)^4 \left(\mathbf{k}_{22}^{1} + \mathbf{k}_{22}^{2} + \mathbf{k}_{22}^{3} + \mathbf{k}_{22}^{4} + \mathbf{k}_{22}^{5} + \mathbf{k}_{22}^{6} + \mathbf{k}_{22}^{7}\right)_{ij} \tag{A.21}$$

The expression for $\mathbf{k}_{22}{}^1$ will be deduced in detail and the results for the remaining expressions follow based on similar arguments.

The equation $i - j - a + b = 0$ can be solved as $i - j = a - b$. Similar to the previous case of $\mathbf{k}_{12}{}^1$, the value and position of $i - j$ can be organized in a matrix:

$$\mathbf{A} = \begin{bmatrix} 0 & -1 & -2 & -3 & \cdots & 1-n \\ 1 & 0 & -1 & -2 & \cdots & 2-n \\ 2 & 1 & 0 & -1 & \cdots & 3-n \\ 3 & 2 & 1 & \ddots & \cdots & 4-n \\ \vdots & \vdots & \vdots & \vdots & \ddots & \vdots \\ n-1 & n-2 & n-3 & n-4 & \cdots & 0 \end{bmatrix} \tag{A.22}$$

From Eq. (A.22) we see that $\mathbf{A} = -\mathbf{A}^T$**.** Along each sub diagonal, $i - j$ takes constant values. Furthermore, $a - b$ are integers like $i - j$ and vary in the same range:

$$i, j, a, b \in \{1, 2, 3 \quad \dots \quad n\} \tag{A.23}$$

Consequently there are equally many combinations of $a - b$ that yield a constant number as there are combinations of $i - j$. Therefore we can conclude that there are n combinations of a's and b's that yield 0, $n - 1$ combinations that yield either 1 or -1 etc. until we only have 1 combination that yields either $1 - n$ or $n - 1$. Given a constant number q:

$$q = i - j \in \{1-n, 2-n, 3-n \quad \dots \quad n-3 \quad n-2 \quad n-1\} \tag{A.24}$$

From relation (A.23) and the fact that each element of $\mathbf{k}_{22}{}^{1}$ involves a double sum over all a and b, we know that for a given *q*, the same *a*'s and *b*'s will combine to *q* regardless of which combinations of *i* and *j* that led to a specified *q*. Consequently, $\mathbf{k}_{22}{}^{1}$ will be constant along all sub-diagonals. Since $\mathbf{k}_{22}{}^{1}$ attains constant values along each sub diagonal, two vectors of values, containing the results for the first row and the first column, hold enough information in order to develop the full matrix. However, since Eq. (A.18) is symmetric in *a* and *b*, $\mathbf{k}_{22}{}^{1}$ is symmetric and hence only one vector, for the purpose of this example the first row in the matrix, needs to be determined in order to have sufficient information to develop the full matrix without further calculations.

By inspection of Eqs. (A.18), (A.19) and (A.22), the following vector is prescribed as the first row:

$$\left(\mathbf{k}^{1}_{22,row}\right)_{n-k+1} = \frac{L}{8}\sum_{j=1}^{k+1} D_{static,j} D_{static,n-k+j-1}\, j^{2}\left(n-k+j-1\right)^{2}, \;\; k \in \{0,1,\ldots,n-1\} \qquad \textbf{(A.25)}$$

Based on eq. (A.25) it can be observed that the calculation of $\mathbf{k}_{22}{}^{1}$ can be performed using $4n(n+1)+1$ flops which is in the order $O(n^2)$ flops. From eq. (A.25) and the above arguments, the explicit expression for $\mathbf{k}_{12}{}^{1}$ can be determined:

$$\mathbf{k}^{1}_{22} = \begin{bmatrix} \left(\mathbf{k}^{1}_{22,row}\right)_{1} & \left(\mathbf{k}^{1}_{22,row}\right)_{2} & \left(\mathbf{k}^{1}_{22,row}\right)_{3} & \left(\mathbf{k}^{1}_{22,row}\right)_{4} & \cdots & \left(\mathbf{k}^{1}_{22,row}\right)_{n} \\ \left(\mathbf{k}^{1}_{22,row}\right)_{2} & \left(\mathbf{k}^{1}_{22,row}\right)_{1} & \left(\mathbf{k}^{1}_{22,row}\right)_{2} & \left(\mathbf{k}^{1}_{22,row}\right)_{3} & \cdots & \left(\mathbf{k}^{1}_{22,row}\right)_{n-1} \\ \left(\mathbf{k}^{1}_{22,row}\right)_{3} & \left(\mathbf{k}^{1}_{22,row}\right)_{2} & \left(\mathbf{k}^{1}_{22,row}\right)_{1} & \left(\mathbf{k}^{1}_{22,row}\right)_{2} & \cdots & \left(\mathbf{k}^{1}_{22,row}\right)_{n-2} \\ \left(\mathbf{k}^{1}_{22,row}\right)_{4} & \left(\mathbf{k}^{1}_{22,row}\right)_{3} & \left(\mathbf{k}^{1}_{22,row}\right)_{2} & \ddots & \cdots & \left(\mathbf{k}^{1}_{22,row}\right)_{n-3} \\ \vdots & \vdots & \vdots & \vdots & \ddots & \vdots \\ \left(\mathbf{k}^{1}_{22,row}\right)_{n} & \left(\mathbf{k}^{1}_{22,row}\right)_{n-1} & \left(\mathbf{k}^{1}_{22,row}\right)_{n-2} & \left(\mathbf{k}^{1}_{22,row}\right)_{n-3} & \cdots & \left(\mathbf{k}^{1}_{22,row}\right)_{1} \end{bmatrix} \qquad \textbf{(A.26)}$$

Expressions for the remaining six matrices $\mathbf{k}_{22}{}^{q}$, $q \in \{2, \quad \ldots \quad 7\}$, can be determined in similar fashions, but their banded structures and symmetric properties vary. The expressions for the remaining six matrices are:

$$\mathbf{k}_{22}^{2}=\mathbf{k}_{22}^{1}$$

$$\mathbf{k}_{22}^{3}=\begin{bmatrix} 0 & & & & & \\ 0 & 0 & & & & \mathbf{0} \\ \left(\mathbf{k}_{22,col}^{3}\right)_{3} & 0 & 0 & & & \\ \vdots & \left(\mathbf{k}_{22,col}^{3}\right)_{3} & 0 & 0 & & \\ \left(\mathbf{k}_{22,col}^{3}\right)_{n-1} & \vdots & \ddots & \ddots & \ddots & \\ \left(\mathbf{k}_{22,col}^{3}\right)_{n} & \left(\mathbf{k}_{22,col}^{3}\right)_{n-1} & \cdots & \left(\mathbf{k}_{22,col}^{3}\right)_{3} & 0 & 0 \end{bmatrix}$$

$$\mathbf{k}_{22}^{4}=\left(\mathbf{k}_{22}^{3}\right)^{T}$$

$$\mathbf{k}_{22}^{5}=\begin{bmatrix} \left(\mathbf{k}_{22,col}^{5}\right)_{1} & \left(\mathbf{k}_{22,col}^{5}\right)_{2} & \cdots & \left(\mathbf{k}_{22,col}^{5}\right)_{n-2} & 0 & 0 \\ \left(\mathbf{k}_{22,col}^{5}\right)_{2} & \vdots & \iddots & 0 & 0 & \\ \vdots & \left(\mathbf{k}_{22,col}^{5}\right)_{n-2} & \iddots & 0 & & \\ \left(\mathbf{k}_{22,col}^{5}\right)_{n-2} & 0 & \iddots & & & \\ 0 & 0 & & & \mathbf{0} & \\ 0 & & & & & \end{bmatrix} \qquad \textbf{(A.27)}$$

$$\mathbf{k}_{22}^{6}=\mathbf{k}_{22}^{5}$$

$$\mathbf{k}_{22}^{7}=\begin{bmatrix} \left(\mathbf{k}_{22,aug}^{7}\right)_{1} & \left(\mathbf{k}_{22,aug}^{7}\right)_{2} & \left(\mathbf{k}_{22,aug}^{7}\right)_{3} & \cdots & \left(\mathbf{k}_{22,aug}^{7}\right)_{n} \\ \left(\mathbf{k}_{22,aug}^{7}\right)_{2} & \left(\mathbf{k}_{22,aug}^{7}\right)_{3} & \ddots & \left(\mathbf{k}_{22,aug}^{7}\right)_{n} & \vdots \\ \left(\mathbf{k}_{22,aug}^{7}\right)_{3} & \vdots & \iddots & \ddots & \left(\mathbf{k}_{22,aug}^{7}\right)_{2n-2} \\ \vdots & \left(\mathbf{k}_{22,aug}^{7}\right)_{n} & \cdots & \left(\mathbf{k}_{22,aug}^{7}\right)_{2n-2} & \left(\mathbf{k}_{22,aug}^{7}\right)_{2n-1} \\ \left(\mathbf{k}_{22,aug}^{7}\right)_{n} & \cdots & \left(\mathbf{k}_{22,aug}^{7}\right)_{2n-2} & \left(\mathbf{k}_{22,aug}^{7}\right)_{2n-1} & \left(\mathbf{k}_{22,aug}^{7}\right)_{2n} \end{bmatrix}$$

The three vectors necessary in order to establish the matrices in eq. (A.26) are determined as follows:

$$\left(\mathbf{k}_{22,col}^{3}\right)_{i}=-\frac{L}{8}\sum_{j=1}^{i-2}D_{static,j}D_{static,i-j-1}j^{2}\left(i-j-1\right)^{2},\ i\in\left\{3,4,\ldots,n\right\}$$

$$\left(\mathbf{k}_{22,col}^{5}\right)_{n-k-1}=-\frac{L}{8}\sum_{j=1}^{k+1}D_{static,j}D_{static,n-k+j-1}j^{2}\left(n-k+j-1\right)^{2},\ k\in\left\{1,2,\ldots,n-2\right\}$$

$$\left(\mathbf{k}_{22,aug}^{7}\right)_{i}=\begin{cases}\dfrac{L}{8}\displaystyle\sum_{j=1}^{i}D_{static,j}D_{static,i-j+1}j^{2}\left(i-j+1\right)^{2}, & i\in\left\{1,2,\ldots,n\right\}\\ \dfrac{L}{8}\displaystyle\sum_{j=i-n+1}^{n}D_{static,j}D_{static,i-j+1}j^{2}\left(i-j+1\right)^{2}, & i\in\left\{n+1,n+2,\ldots,2n-1\right\}\end{cases} \qquad \textbf{(A.28)}$$

APPENDIX B

We will derive the expression for the tangential strain, given in Eq. (14). The first part of the derivation, determining the expressions for general curvilinear coordinates, is to a large extent based on the derivation given by Axissa and Trompette [2005].

It is assumed that a curvilinear coordinate system is defined by two families of orthogonal curves C_α and C_β. In a Cartesian coordinate system the curves are defined by the parametric equation

$$\mathbf{r}(\alpha,\beta) = x(\alpha,\beta)\mathbf{i} + y(\alpha,\beta)\mathbf{j} \tag{B.1}$$

When setting α equal to a constant Eq. (B.1) describes the curves C_α, and the curves C_β are defined in the same manner by setting β to a constant. An example of a coordinate system is illustrated in Fig. B1 below.

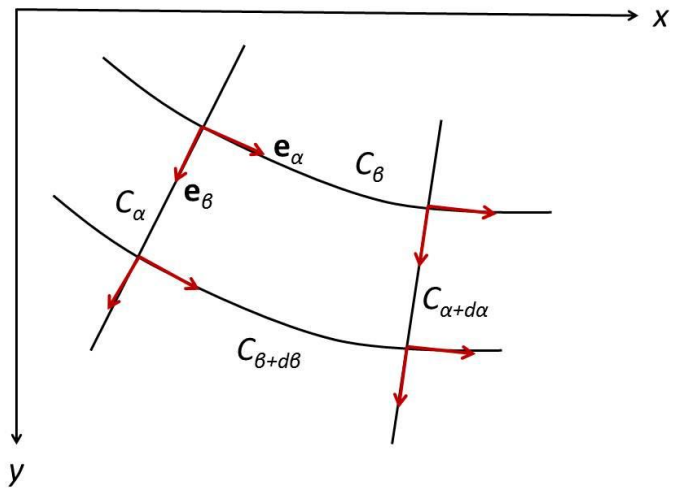

Figure B1 – A curvilinear coordinate system with orthonormal unit vectors.

Differentiating with regard to α one obtains the vector

$$\mathbf{t}_\alpha = \frac{\partial \mathbf{r}}{\partial \alpha} = \frac{\partial x}{\partial \alpha}\mathbf{i} + \frac{\partial y}{\partial \alpha}\mathbf{j} \tag{B.2}$$

which for each value of β describes a set of vectors that are tangential to the corresponding curve C_β. A unit vector $\mathbf{e}_\alpha$ may then be formed by setting

$$\mathbf{t}_\alpha = g_\alpha \mathbf{e}_\alpha, \quad \text{where} \quad g_\alpha = |\mathbf{t}_\alpha| = \sqrt{\left(\frac{\partial x}{\partial \alpha}\right)^2 + \left(\frac{\partial y}{\partial \alpha}\right)^2} \tag{B.3}$$

Accordingly

$$\mathbf{t}_\beta = \frac{\partial \mathbf{r}}{\partial \beta} = \frac{\partial x}{\partial \beta}\mathbf{i} + \frac{\partial y}{\partial \beta}\mathbf{j} = g_\beta \mathbf{e}_\beta, \quad \text{where} \quad g_\beta = |\mathbf{t}_\beta| = \sqrt{\left(\frac{\partial x}{\partial \beta}\right)^2 + \left(\frac{\partial y}{\partial \beta}\right)^2} \tag{B.4}$$

By definition the unit vectors $\mathbf{e}_\alpha$ and $\mathbf{e}_\beta$ are orthogonal. Hence

$$\begin{aligned} &\mathbf{t}_\alpha \cdot \mathbf{t}_\beta = \frac{1}{g_\alpha g_\beta}\left(\frac{\partial x}{\partial \alpha}\mathbf{i} + \frac{\partial y}{\partial \alpha}\mathbf{j}\right) \cdot \left(\frac{\partial x}{\partial \beta}\mathbf{i} + \frac{\partial y}{\partial \beta}\mathbf{j}\right) = 0 \\ &\Rightarrow \frac{\partial x}{\partial \alpha}\frac{\partial x}{\partial \beta} + \frac{\partial y}{\partial \alpha}\frac{\partial y}{\partial \beta} = 0 \end{aligned} \tag{B.5}$$

Applying this result as well as the invariance (between coordinate systems) of a general infinitesimal segment ds_g one obtains

$$\begin{aligned} ds_g{}^2 = dx^2 + dy^2 &= \left(\frac{\partial x}{\partial \alpha}d\alpha + \frac{\partial x}{\partial \beta}d\beta\right)^2 + \left(\frac{\partial y}{\partial \alpha}d\alpha + \frac{\partial y}{\partial \beta}d\beta\right)^2 \\ &= \left(\left(\frac{\partial x}{\partial \alpha}\right)^2 + \left(\frac{\partial y}{\partial \alpha}\right)^2\right)d\alpha^2 + \left(\left(\frac{\partial x}{\partial \beta}\right)^2 + \left(\frac{\partial y}{\partial \beta}\right)^2\right)d\beta^2 = g_\alpha{}^2 d\alpha^2 + g_\beta{}^2 d\beta^2 \end{aligned} \tag{B.6}$$

This can be reformulated as a matrix equation

$$ds_g{}^2 = \begin{bmatrix} dx & dy \end{bmatrix}\begin{bmatrix} 1 & 0 \\ 0 & 1 \end{bmatrix}\begin{bmatrix} dx \\ dy \end{bmatrix} = \begin{bmatrix} d\alpha & d\beta \end{bmatrix}\begin{bmatrix} g_\alpha{}^2 & 0 \\ 0 & g_\beta{}^2 \end{bmatrix}\begin{bmatrix} d\alpha \\ d\beta \end{bmatrix} \tag{B.7}$$

The square matrices in Eq.(B.7) are the metric tensors in Cartesian coordinates and orthonormal curvilinear coordinates, respectively.

Next, we are aiming to determine the rate of change of the unit vectors $\mathbf{e}_\alpha$ and $\mathbf{e}_\beta$. In order to accomplish this the orthonormal properties of the unit vectors are utilized. First, we note that

$$\mathbf{e}_\alpha \cdot \mathbf{e}_\alpha = 1 \quad \Rightarrow \quad \mathbf{e}_\alpha \cdot \frac{\partial \mathbf{e}_\alpha}{\partial \alpha} = 0 \quad \Rightarrow \quad \frac{\partial \mathbf{e}_\alpha}{\partial \alpha} = a \cdot \mathbf{e}_\beta \tag{B.8}$$

Where a is a scalar. In Eq. (B.8) the second statement follows by differentiating the first with regard to α, and the third statement follows because any vector in this two-dimensional treatment is orthogonal to the unit vector $\mathbf{e}_\alpha$ if and only if it is parallel with the other unit vector $\mathbf{e}_\beta$.

Similarly

$$\mathbf{e}_\alpha \cdot \mathbf{e}_\alpha = 1 \quad \Rightarrow \quad \mathbf{e}_\alpha \cdot \frac{\partial \mathbf{e}_\alpha}{\partial \beta} = 0 \quad \Rightarrow \quad \frac{\partial \mathbf{e}_\alpha}{\partial \beta} = b \cdot \mathbf{e}_\beta \tag{B.9}$$

Furthermore, it follows from differentiation of the orthogonal relation below that

$$\mathbf{e}_\alpha \cdot \mathbf{e}_\beta = 0 \quad \Rightarrow \quad \mathbf{e}_\alpha \cdot \frac{\partial \mathbf{e}_\beta}{\partial \alpha} = -\frac{\partial \mathbf{e}_\alpha}{\partial \alpha} \cdot \mathbf{e}_\beta = -a \tag{B.10}$$

From Eqs. (B.1)-(B.4) we know that differentiating a position vector $\mathbf{r}$ yields

$$\frac{\partial \mathbf{r}}{\partial \alpha} = g_\alpha \mathbf{e}_\alpha \quad \wedge \quad \frac{\partial \mathbf{r}}{\partial \beta} = g_\beta \mathbf{e}_\beta \tag{B.11}$$

The equality of the mixed partial derivatives imply

$$\frac{\partial^2 \mathbf{r}}{\partial \alpha \, \partial \beta} = \frac{\partial g_\alpha}{\partial \beta} \mathbf{e}_\alpha + g_\alpha \frac{\partial \mathbf{e}_\alpha}{\partial \beta} = \frac{\partial g_\beta}{\partial \alpha} \mathbf{e}_\beta + g_\beta \frac{\partial \mathbf{e}_\beta}{\partial \alpha} \tag{B.12}$$

Now dot-multiplying the above with $\mathbf{e}_\alpha$ and utilizing again the orthonormal properties of the unit vectors as well as Eqs. (B.9) and (B.10), we get

$$\frac{\partial g_\alpha}{\partial \beta} = g_\beta \frac{\partial \mathbf{e}_\beta}{\partial \alpha} \cdot \mathbf{e}_\alpha = -a g_\beta \quad \Rightarrow \quad a = -\frac{1}{g_\beta} \frac{\partial g_\alpha}{\partial \beta} \tag{B.13}$$

Hence, it follows from Eq. (B.8) that

$$\frac{\partial \mathbf{e}_\alpha}{\partial \alpha} = a \cdot \mathbf{e}_\beta = -\frac{1}{g_\beta} \frac{\partial g_\alpha}{\partial \beta} \mathbf{e}_\beta \tag{B.14}$$

Subsequently we can determine an expression for the derivative of the other unit vector $\mathbf{e}_\beta$ with regard to α using the following relation:

$$\mathbf{e}_\beta \cdot \mathbf{e}_\beta = 1 \quad \Rightarrow \quad \mathbf{e}_\beta \cdot \frac{\partial \mathbf{e}_\beta}{\partial \alpha} = 0 \quad \Rightarrow \quad \frac{\partial \mathbf{e}_\beta}{\partial \alpha} = c \cdot \mathbf{e}_\alpha \tag{B.15}$$

In conjunction with Eq. (B.10) we get

$$\mathbf{e}_\alpha \cdot \frac{\partial \mathbf{e}_\beta}{\partial \alpha} = c = -a \quad \Rightarrow \quad \frac{\partial \mathbf{e}_\beta}{\partial \alpha} = \frac{1}{g_\beta}\frac{\partial g_\alpha}{\partial \beta}\mathbf{e}_\alpha \tag{B.16}$$

The two remaining derivatives may be obtained in a similar manner. The results are summarized in the matrix below:

$$\begin{bmatrix} \frac{\partial \mathbf{e}_\alpha}{\partial \alpha} & \frac{\partial \mathbf{e}_\alpha}{\partial \beta} \\ \frac{\partial \mathbf{e}_\beta}{\partial \alpha} & \frac{\partial \mathbf{e}_\beta}{\partial \beta} \end{bmatrix} = \begin{bmatrix} -\frac{1}{g_\beta}\frac{\partial g_\alpha}{\partial \beta}\mathbf{e}_\beta & \frac{1}{g_\alpha}\frac{\partial g_\beta}{\partial \alpha}\mathbf{e}_\beta \\ \frac{1}{g_\beta}\frac{\partial g_\alpha}{\partial \beta}\mathbf{e}_\alpha & -\frac{1}{g_\alpha}\frac{\partial g_\beta}{\partial \alpha}\mathbf{e}_\alpha \end{bmatrix} \tag{B.17}$$

The gradient operator may be determined by inspecting the gradient of a scalar field $\Phi(x,y)$:

$$\nabla\Phi = \frac{\partial \Phi}{\partial x}\mathbf{i} + \frac{\partial \Phi}{\partial y}\mathbf{j} = G_\alpha \mathbf{e}_\alpha + G_\beta \mathbf{e}_\beta \tag{B.18}$$

Once more utilizing the orthonormal properties of $\mathbf{e}_\alpha$ and $\mathbf{e}_\beta$ as well as Eqs. (B.2) and (B.3), we obtain

$$\begin{aligned} G_\alpha &= \left(\frac{\partial \Phi}{\partial x}\mathbf{i} + \frac{\partial \Phi}{\partial y}\mathbf{j}\right)\cdot \mathbf{e}_\alpha = \frac{1}{g_\alpha}\left(\frac{\partial \Phi}{\partial x}\mathbf{i} + \frac{\partial \Phi}{\partial y}\mathbf{j}\right)\cdot\left(\frac{\partial x}{\partial \alpha}\mathbf{i} + \frac{\partial y}{\partial \alpha}\mathbf{j}\right) = \frac{1}{g_\alpha}\left(\frac{\partial x}{\partial \alpha}\frac{\partial \Phi}{\partial x} + \frac{\partial y}{\partial \alpha}\frac{\partial \Phi}{\partial y}\right) \\ &= \frac{1}{g_\alpha}\frac{\partial \Phi}{\partial \alpha} \end{aligned} \tag{B.19}$$

Similarly

$$G_\beta = \left(\frac{\partial \Phi}{\partial x}\mathbf{i} + \frac{\partial \Phi}{\partial y}\mathbf{j}\right)\cdot \mathbf{e}_\beta = \frac{1}{g_\beta}\frac{\partial \Phi}{\partial \beta} \tag{B.20}$$

Thus the gradient operator for the orthonormal curvilinear coordinate system is

$$\nabla = \mathbf{e}_\alpha \frac{1}{g_\alpha}\frac{\partial}{\partial \alpha} + \mathbf{e}_\beta \frac{1}{g_\beta}\frac{\partial}{\partial \beta} \tag{B.21}$$

Because $\mathbf{e}_\alpha$ and $\mathbf{e}_\beta$ are orthonormal the dyadic products involving the two unit vectors may be represented by square matrices with all entries equal to zero except the entry at the row corresponding to the first subscript and column corresponding to the second subscript, which will have unit value, i.e.,

$$\mathbf{e}_\alpha\mathbf{e}_\alpha=\begin{bmatrix}1 & 0\\ 0 & 0\end{bmatrix},\quad \mathbf{e}_\alpha\mathbf{e}_\beta=\begin{bmatrix}0 & 1\\ 0 & 0\end{bmatrix},\quad \mathbf{e}_\beta\mathbf{e}_\alpha=\begin{bmatrix}0 & 0\\ 1 & 0\end{bmatrix},\quad \mathbf{e}_\beta\mathbf{e}_\beta=\begin{bmatrix}0 & 0\\ 0 & 1\end{bmatrix} \tag{B.22}$$

Consequently, the gradient of a vector field **X** may be determined by

$$\nabla\mathbf{X}=\left(\mathbf{e}_\alpha\frac{1}{g_\alpha}\frac{\partial}{\partial\alpha}+\mathbf{e}_\beta\frac{1}{g_\beta}\frac{\partial}{\partial\beta}\right)\left(X_\alpha\mathbf{e}_\alpha+X_\beta\mathbf{e}_\beta\right) \tag{B.23}$$

The components of this matrix can be calculated with the aid of Eq. (B.17):

$$\begin{aligned}\mathbf{e}_\alpha\frac{1}{g_\alpha}\frac{\partial}{\partial\alpha}\left(X_\alpha\mathbf{e}_\alpha\right)&=\frac{1}{g_\alpha}\frac{\partial X_\alpha}{\partial\alpha}\mathbf{e}_\alpha\mathbf{e}_\alpha+\frac{X_\alpha}{g_\alpha}\mathbf{e}_\alpha\frac{\partial\mathbf{e}_\alpha}{\partial\alpha}\\&=\frac{1}{g_\alpha}\frac{\partial X_\alpha}{\partial\alpha}\mathbf{e}_\alpha\mathbf{e}_\alpha-\frac{X_\alpha}{g_\alpha g_\beta}\frac{\partial g_\alpha}{\partial\beta}\mathbf{e}_\alpha\mathbf{e}_\beta\end{aligned} \tag{B.24}$$

$$\begin{aligned}\mathbf{e}_\beta\frac{1}{g_\beta}\frac{\partial}{\partial\beta}\left(X_\alpha\mathbf{e}_\alpha\right)&=\frac{1}{g_\beta}\frac{\partial X_\alpha}{\partial\beta}\mathbf{e}_\beta\mathbf{e}_\alpha+\frac{X_\alpha}{g_\beta}\mathbf{e}_\beta\frac{\partial\mathbf{e}_\alpha}{\partial\beta}\\&=\frac{1}{g_\beta}\frac{\partial X_\alpha}{\partial\beta}\mathbf{e}_\beta\mathbf{e}_\alpha+\frac{X_\alpha}{g_\alpha g_\beta}\frac{\partial g_\beta}{\partial\alpha}\mathbf{e}_\beta\mathbf{e}_\beta\end{aligned} \tag{B.25}$$

$$\begin{aligned}\mathbf{e}_\alpha\frac{1}{g_\alpha}\frac{\partial}{\partial\alpha}\left(X_\beta\mathbf{e}_\beta\right)&=\frac{1}{g_\alpha}\frac{\partial X_\beta}{\partial\alpha}\mathbf{e}_\alpha\mathbf{e}_\beta+\frac{X_\beta}{g_\alpha}\mathbf{e}_\alpha\frac{\partial\mathbf{e}_\beta}{\partial\alpha}\\&=\frac{1}{g_\alpha}\frac{\partial X_\beta}{\partial\alpha}\mathbf{e}_\alpha\mathbf{e}_\beta+\frac{X_\beta}{g_\alpha g_\beta}\frac{\partial g_\alpha}{\partial\beta}\mathbf{e}_\alpha\mathbf{e}_\alpha\end{aligned} \tag{B.26}$$

$$\begin{aligned}\mathbf{e}_\beta\frac{1}{g_\beta}\frac{\partial}{\partial\beta}\left(X_\beta\mathbf{e}_\beta\right)&=\frac{1}{g_\beta}\frac{\partial X_\beta}{\partial\beta}\mathbf{e}_\beta\mathbf{e}_\beta+\frac{X_\beta}{g_\beta}\mathbf{e}_\beta\frac{\partial\mathbf{e}_\beta}{\partial\beta}\\&=\frac{1}{g_\beta}\frac{\partial X_\beta}{\partial\beta}\mathbf{e}_\beta\mathbf{e}_\beta-\frac{X_\beta}{g_\alpha g_\beta}\frac{\partial g_\beta}{\partial\alpha}\mathbf{e}_\beta\mathbf{e}_\alpha\end{aligned} \tag{B.27}$$

Inserting the matrices from Eq. (B.22) into Eqs. (B.24)-(B.27) and adding the terms according to Eq. (B.23) one obtains

$$\nabla \mathbf{X} = \begin{bmatrix} \frac{1}{g_\alpha}\frac{\partial X_\alpha}{\partial \alpha} + \frac{X_\beta}{g_\alpha g_\beta}\frac{\partial g_\alpha}{\partial \beta} & \frac{1}{g_\alpha}\frac{\partial X_\beta}{\partial \alpha} - \frac{X_\alpha}{g_\alpha g_\beta}\frac{\partial g_\alpha}{\partial \beta} \\ \frac{1}{g_\beta}\frac{\partial X_\alpha}{\partial \beta} - \frac{X_\beta}{g_\alpha g_\beta}\frac{\partial g_\beta}{\partial \alpha} & \frac{1}{g_\beta}\frac{\partial X_\beta}{\partial \beta} + \frac{X_\alpha}{g_\alpha g_\beta}\frac{\partial g_\beta}{\partial \alpha} \end{bmatrix} \quad \textbf{(B.28)}$$

Now if the metric tensor and the displacement field **u** in the curvilinear coordinate system displayed in Fig. 5 are known, the strain tensor $\boldsymbol{\varepsilon}$ may be calculated:

$$\varepsilon = \frac{1}{2}\left(\nabla \mathbf{u} + (\nabla \mathbf{u})^T\right) = \begin{bmatrix} \varepsilon_{ss} & \varepsilon_{sn} \\ \varepsilon_{ns} & \varepsilon_{nn} \end{bmatrix} \quad \textbf{(B.29)}$$

From Fig. B2 below it may be seen that an infinitesimal element in the curvilinear system has side length equal to $(1+n/R)ds$ in the tangential direction, where R is the radius of curvature. In the perpendicular direction the side length of an infinitesimal element is dn.

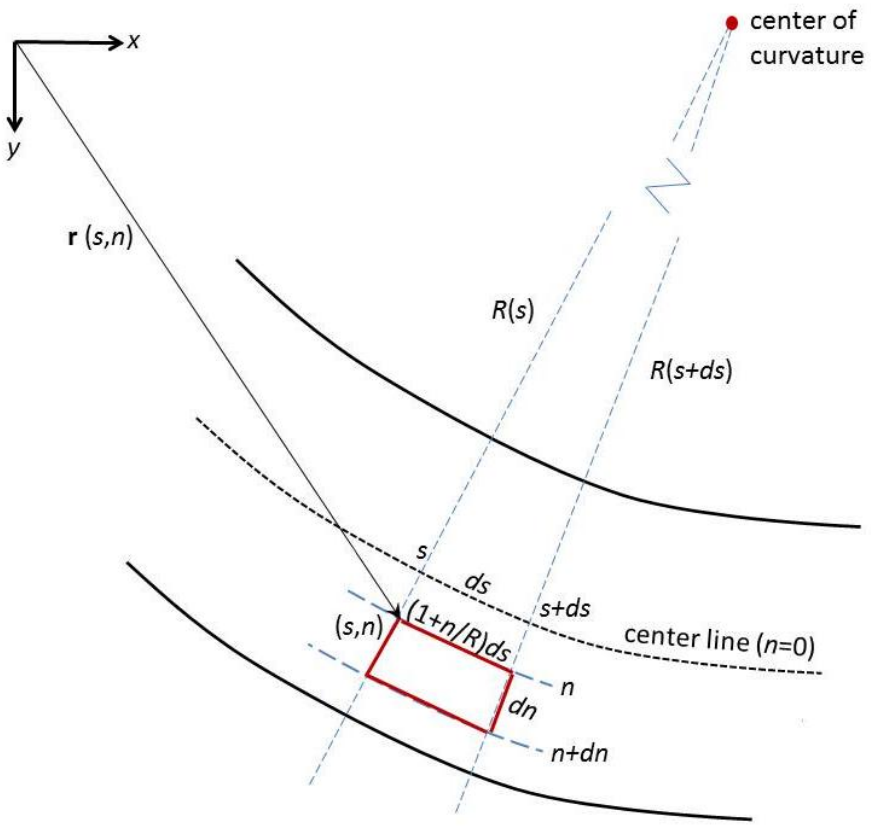

Figure B2 – Infinitesimal element in the curvilinear coordinate system.

Hence, we can determine the metric tensor through the relation

$$ds_g{}^2 = (1+\frac{n}{R})^2 ds^2 + dn^2 = \begin{bmatrix} ds & dn \end{bmatrix} \begin{bmatrix} (1+n/R)^2 & 0 \\ 0 & 1 \end{bmatrix} \begin{bmatrix} ds \\ dn \end{bmatrix} = \begin{bmatrix} ds & dn \end{bmatrix} \begin{bmatrix} g_s{}^2 & 0 \\ 0 & g_n{}^2 \end{bmatrix} \begin{bmatrix} ds \\ dn \end{bmatrix}$$

$$\Rightarrow \quad g_s = 1+\frac{n}{R} \quad \wedge \quad g_n = 1 \tag{B.30}$$

The unit vector pairs (**i**,**j**) in the *x*- and *y*-directions and ($\mathbf{e}_s$,$\mathbf{e}_n$) in tangential and normal directions are both clockwise, as shown in Fig. 5 and Fig. B2. Assuming the radius of curvature *R* to always be positive by definition, it should be noted that $g_s = (1 - n/R)$ when the initial pipeline curvature is opposite relative to the situation in Fig. B2.

The initial curvature κ in cross-flow direction is calculated by Eq. (11). From Eqs. (9) and (11) and inspection of Figs. 5 and B2 it is clear that the curvature κ will be positive when $\mathbf{e}_n$ points towards the center of curvature. The metric tensor for the ($\mathbf{e}_s$,$\mathbf{e}_n$) system can now be uniquely determined for all curvatures by setting

$$g_s = 1-\kappa n \quad \wedge \quad g_n = 1 \tag{B.31}$$

Now we need to determine the displacement field **u**. The cross-flow plane (the plane of initial curvature) is assumed to be a plane of symmetry and the *z*-direction may be ignored, i.e. there will be no displacement in this direction for pure cross-flow oscillations. Consequently, the displacement will have two components:

$$\mathbf{u} = u_s \mathbf{e}_s + u_n \mathbf{e}_n \tag{B.32}$$

Using Euler-Bernoulli beam theory and Navier's hypothesis, it is assumed that plane sections remain plane and perpendicular to the neutral axis and that displacements are small. The displacements of an arbitrary point on the cross section can thus be expressed in terms of the displacements of points on the center line. As mentioned in Section 3.2, the eccentricity of the neutral axis relative to the center line and the deviation from a linear bending stress distribution in case of pure bending (i.e., not subjected to axial force) are small for the ranges of diameters and curvatures of interest. Expressions for the stress distribution and position of the neutral axis in curved beams with circular cross-sections are given e.g., by Srivastava and Gope [2007].

In the perpendicular direction all the points on a cross section displaces an equal amount when excluding the second order transversal displacement due to rotation of the cross section, i.e.,

$$u_n(s,n) = v_0(s) \tag{B.33}$$

where v_0 is the displacement of points on the center line, consistent with the notation used in Eq. (13).

The tangential displacement will consist of two components. Firstly the displacement u_b due to bending, and secondly the displacement u_c of a point a distance n from the centroidal axis due to the corresponding displacement u_0 of a point on the center line. The displacement due to bending will have the familiar form [Shames and Dym, 1996])

$$u_b(s,n) = -n\phi(s) \tag{B.34}$$

where ϕ is the bending rotation of the cross section.

Note, as discussed previously with regard to Eq. (13), that including a curvature-dependent term in the second component of the tangential displacement is not required, but making this provision is convenient since it causes the shear strains to vanish. Furthermore, it is quite natural to assume that the cross-section rotates in such a manner that the curved geometry of the infinitesimal beam segment is preserved whenever a tangential displacement of the centroid occurs. This assumption will have the same effect on the displacement field as treating the displacements u_0 of points on the centroidal axis as circumferential rather than purely tangential, in conjunction with applying the assumption that cross-sections remain plane and normal to the centroidal axis [Kirkhope, 1977]. The second displacement component, when regarded in the latter way, is illustrated in Fig. B3 below, where we are looking at an infinitesimal beam segment that experiences a circumferential displacement u_0 for points along the center line. The blue lines mark the cross-sections that constitute the boundaries of the infinitesimal segment prior to deformation, while the red lines mark the boundaries of the segment subsequent to deformation. If we now focus on the distance between the left segment boundaries, the distance is per definition u_0 at the center line. However, for $n > 0$ the distance will, if plane sections remain plane, be larger than u_0 when $\kappa < 0$. From geometric consideration of Figs. B2 and B3 it will be given by $(1 - \kappa n)u_0$.

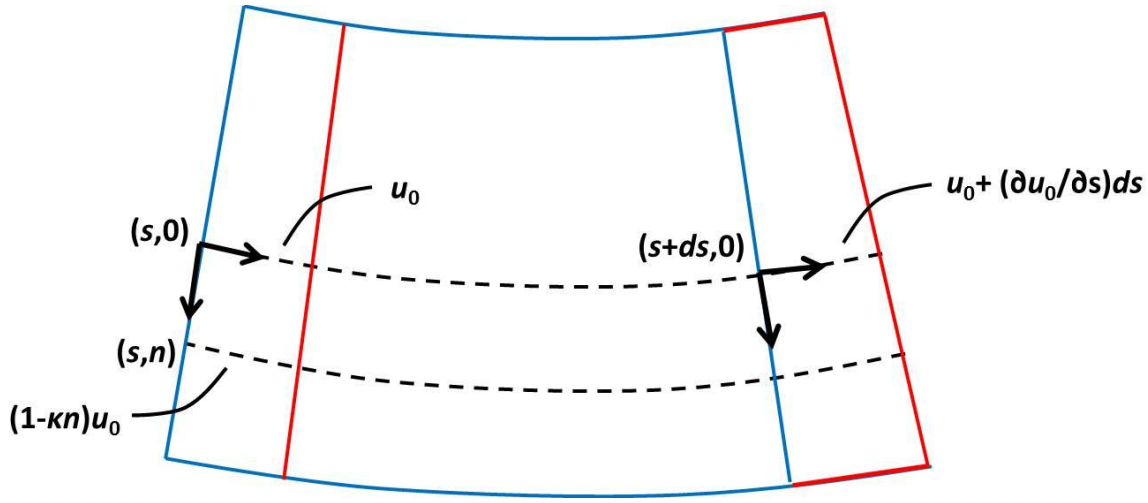

Figure B3 – Circumferential displacement of an infinitesimal beam element

This relationship applies also for $n < 0$ and $\kappa > 0$. Thus we get

$$u_c(s,n) = (1-\kappa(s)n)u_0(s) \tag{B.35}$$

Adding the two terms gives the total tangential displacement

$$u_s(s,n) = u_b + u_c = u_0(s) - n(\phi(s) + \kappa(s)u_0(s)) \tag{B.36}$$

Now that both the metric tensor and the displacement field are known the strain tensor may be calculated. First we apply Eq. (B.28) to determine

$$\nabla\mathbf{u} = \begin{bmatrix} \frac{1}{1-\kappa n}\left(\frac{\partial u_s}{\partial s} - \kappa u_n\right) & \frac{1}{1-\kappa n}\left(\frac{\partial u_n}{\partial s} + \kappa u_s\right) \\ \frac{\partial u_s}{\partial n} & \frac{\partial u_n}{\partial n} \end{bmatrix} \tag{B.37}$$

The strain tensor is then readily calculated using Eq. (B.29), and substituting Eqs. (B.33) and (B.36) into Eq. (B.37):

$$\varepsilon = \begin{bmatrix} \varepsilon_{ss} & \varepsilon_{sn} \\ \varepsilon_{ns} & \varepsilon_{nn} \end{bmatrix} = \begin{bmatrix} \dfrac{1}{1-\kappa n}\left(\dfrac{\partial u_s}{\partial s} - \kappa u_n\right) & \dfrac{1}{2}\left(\dfrac{\partial u_s}{\partial n} + \dfrac{1}{1-\kappa n}\left(\dfrac{\partial u_n}{\partial s} + \kappa u_s\right)\right) \\ \dfrac{1}{2}\left(\dfrac{\partial u_s}{\partial n} + \dfrac{1}{1-\kappa n}\left(\dfrac{\partial u_n}{\partial s} - \kappa u_s\right)\right) & \dfrac{\partial u_n}{\partial n} \end{bmatrix}$$
$$= \begin{bmatrix} \dfrac{1}{1-\kappa n}\left(\dfrac{\partial u_0}{\partial s} - \kappa v_0 - n\dfrac{\partial}{\partial s}(\phi + \kappa u_0)\right) & \dfrac{1}{2}\left(\dfrac{1}{1-\kappa n}\left(\dfrac{\partial v_0}{\partial s} - \phi\right)\right) \\ \dfrac{1}{2}\left(\dfrac{1}{1-\kappa n}\left(\dfrac{\partial v_0}{\partial s} - \phi\right)\right) & 0 \end{bmatrix} \quad \textbf{(B.38)}$$

We have further assumed that the average shear angle $\theta = (\partial v_0/\partial s - \phi)$ is approximately zero. Hence, for our purposes we may set:

$$\phi \approx \frac{\partial v_0}{\partial s} \quad \Rightarrow \quad \varepsilon = \begin{bmatrix} \varepsilon_{ss} & \varepsilon_{sn} \\ \varepsilon_{ns} & \varepsilon_{nn} \end{bmatrix} = \begin{bmatrix} \dfrac{1}{1-\kappa n}\left(\dfrac{\partial u_0}{\partial s} - \kappa v_0 - n\dfrac{\partial}{\partial s}\left(\dfrac{\partial v_0}{\partial s} + \kappa u_0\right)\right) & 0 \\ 0 & 0 \end{bmatrix} \quad \textbf{(B.39)}$$

We will examine the validity of assuming negligible shear by comparing results from the semi-analytical model to results from FE analyses performed with Kirchoff beam elements including shear effects. Finally, it is observed from Eq. (B.40) that the tangential strain component ε_{ss} now gets the form presented in Eq. (14), which is what we wanted to show. This expression is also consistent with tangential strain expressions applied elsewhere in the literature [Kirkhope, 1977; Charpie, 1991; Charpie and Burroughs, 1993; Tarnopolskaya et al., 1996; Wu, 2009].

APPENDIX C

Table C.1 – Input data and comparison of results from FE and semi-analytical method for verification cases 1-7.

Input	Unit	Case 1	Case 2	Case 3	Case 4	Case 5	Case 6	Case 7
L_s	m	125	125	125	175	75	75	75
$L_{shoulder}$		375	375	375	525	225	225	225
L_{elem}		0.1	0.1	0.1	0.1	0.1	0.1	0.1
K_{VS}	MN/m^2	1.30	1.30	1.30	1.30	1.30	1.30	1.30
K_V		12.0	12.0	12.0	12.0	12.0	12.0	12.0
K_L, K_{AX}		8.29	8.29	8.29	8.29	8.29	8.29	8.29
D_s	m	1	1	1	1	1	1	1
t_s	m	0.03	0.03	0.03	0.03	0.03	0.03	0.03
q	N/m	5539	1055	1055	1055	1055	1055	1055
m_e	kg/m	2178	1721	1721	1721	1721	1721	1721
$S_{eff,i}$	kN	0	-1500	-3500	3500	2000	0	-2000
E	GPa	207	207	207	207	207	207	207
ν	-	0.29	0.29	0.29	0.29	0.29	0.29	0.29
Results, FE								
$f_{IL,1}$	Hz	0.220	0.184	0.140	0.178	0.577	0.535	0.488
$f_{IL,2}$		0.567	0.553	0.504	0.413	1.520	1.462	1.402
$f_{IL,3}$		1.049	1.117	1.067	0.734	1.966*/ 2.885	1.966*/ 2.824	1.9661*/ 2.7605
$f_{CF,1}$		0.370	0.227	0.283	0.191	0.594	0.553	0.507
$f_{CF,2}$		0.577	0.565	0.516	0.418	1.567	1.509	1.448
$f_{CF,3}$		1.074	1.142	1.102	0.744	2.988	2.924	2.859
$A_{IL,1}$	MPa	126.5	116.8	110.9	82.4	268.9	263.7	260.3
$A_{IL,2}$		303.4	291.6	294.9	193.2	702.1	706.6	711.6
$A_{IL,3}$		603.0	559.2	605.2	323.4	1447.9	1452.4	1455.6
$A_{CF,1}$		159.0	126.6	138.5	87.5	286.6	282.7	278.4
$A_{CF,2}$		324.7	314.7	308.7	204.0	725.5	730.0	734.5
$A_{CF,3}$		602.0	619.6	634.5	346.5	1505.1	1508.3	1511.5
S_{eff}	kN	1510	-1300	-2740	3590	2010	8.18	-1990
δ/D_s	-	2.04	0.746	1.44	0.695	0.0798	0.0951	0.118
Time	s	100.6	102.2	131.5	103.1	95.6	94.8	94.5
Results, Semi-Analytical								
$f_{IL,1}$	Hz	0.221	0.186	0.142	0.178	0.582	0.540	0.494
$f_{IL,2}$		0.571	0.557	0.508	0.415	1.535	1.477	1.416
$f_{IL,3}$		1.082	1.125	1.074	0.738	2.923	2.860	2.795
$f_{CF,1}$		0.371	0.227	0.282	0.191	0.597	0.554	0.509
$f_{CF,2}$		0.579	0.567	0.517	0.419	1.574	1.516	1.455
$f_{CF,3}$		1.107	1.147	1.106	0.745	3.007	2.944	2.878
$A_{IL,1}$	MPa	127.5	117.6	112.1	82.2	273.6	270.1	266.3
$A_{IL,2}$		308.7	300.3	297.1	193.2	710.8	715.2	719.7
$A_{IL,3}$		605.9	609.0	611.0	326.7	1474.8	1477.8	1480.7
$A_{CF,1}$		158.3	125.8	138.0	86.1	288.2	283.9	279.3
$A_{CF,2}$		323.7	313.8	309.7	199.5	730.8	735.0	739.3
$A_{CF,3}$		633.3	622.6	637.6	340.4	1520.9	1524.0	1527.1
S_{eff}	kN	1510	-1300	-2750	3590	2010	8.08	-1990
δ/D_s	-	2.04	0.743	1.428	0.696	0.0797	0.0948	0.117
# inc.	-	1	1	10	1	1	1	1
# sinus	-	220	220	420	220	220	220	220
Time	s	0.21	0.21	12.75	0.21	0.21	0.21	0.21

* The indicated frequency represents shear mode, see discussion in Section 6.1

Table C.2 – Input data and comparison of results from FE and semi-analytical method for verification cases 8-14.

Input	Unit	Case 8	Case 9	Case 10	Case 11	Case 12	Case 13	Case 14
L_s	m	75	20	30	40	20	30	40
$L_{shoulder}$		225	60	90	120	60	90	120
L_{elem}		0.1	0.01683	0.01683	0.01683	0.01683	0.01683	0.01683
K_{VS}	MN/m^2	1.30	0.210	0.210	0.210	1.35	1.35	1.35
K_V		12.0	2.41	2.41	2.41	30.6	30.6	30.6
K_L, K_{AX}		8.29	1.65	1.65	1.65	23.0	23.0	23.0
D_s	m	1	0.1683	0.1683	0.1683	0.1683	0.1683	0.1683
t_s	m	0.03	0.0183	0.0183	0.0183	0.0183	0.0183	0.0183
q	N/m	1055	664.1	664.1	664.1	664.1	664.1	664.1
m_e	kg/m	1721	90.5	90.5	90.5	90.5	90.5	90.5
$S_{eff,i}$	kN	-8000	0	0	0	0	0	0
E	GPa	207	207	207	207	207	207	207
v	-	0.29	0.29	0.29	0.29	0.29	0.29	0.29
Results, FE								
$f_{IL,1}$	Hz	0.308	1.520	0.884	0.656	1.761	0.944	0.679
$f_{IL,2}$		1.204	4.062	2.223	1.532	4.804	2.431	1.615
$f_{IL,3}$		1.966*/ 2.564	7.711	4.142	2.727	9.346	4.610	2.917
$f_{CF,1}$		0.366	1.727	1.361	1.278	1.994	1.664	1.600
$f_{CF,2}$		1.250	4.223	2.277	1.558	4.884	2.458	1.627
$f_{CF,3}$		2.659	8.005	4.272	2.796	9.509	4.696	2.989
$A_{IL,1}$	MPa	248.3	84.1	49.5	35.7	120.1	64.1	43.1
$A_{IL,2}$		726.9	237.6	118.7	78.3	292.7	160.9	105.2
$A_{IL,3}$		1468.2	483.5	249.0	148.6	598.4	283.7	193.2
$A_{CF,1}$		265.7	92.0	57.6	47.0	127.1	83.7	84.2
$A_{CF,2}$		749.0	248.1	122.2	84.6	309.4	167.4	108.9
$A_{CF,3}$		1521.8	511.5	261.2	153.0	610.2	295.9	166.8
S_{eff}	kN	-7830	26.2	84.2	139	15.2	66.8	124
δ/D_s	-	0.424	0.928	2.34	3.88	0.651	1.94	3.52
Time	s	112.7	125.5	139.5	199.0	128.3	141.9	201.7
Results, Semi-Analytical								
$f_{IL,1}$	Hz	0.316	1.538	0.898	0.658	1.782	0.952	0.681
$f_{IL,2}$		1.218	4.118	2.255	1.541	4.860	2.455	1.624
$f_{IL,3}$		2.595	7.837	4.202	2.749	9.460	4.660	2.938
$f_{CF,1}$		0.367	1.732	1.372	1.270	2.001	1.663	1.593
$f_{CF,2}$		1.257	4.249	2.276	1.562	4.923	2.473	1.632
$f_{CF,3}$		2.679	8.142	4.286	2.808	9.595	4.732	3.004
$A_{IL,1}$	MPa	253.2	87.0	50.7	35.0	121.6	64.1	43.5
$A_{IL,2}$		734.2	242.9	121.2	79.8	297.4	160.2	106.4
$A_{IL,3}$		1488.3	497.3	254.5	151.9	611.3	289.4	185.4
$A_{CF,1}$		266.5	93.1	57.9	46.4	126.8	81.6	82.5
$A_{CF,2}$		753.7	251.6	124.3	83.9	309.0	164.3	108.4
$A_{CF,3}$		1539.9	519.5	265.7	155.6	621.2	300.6	167.3
S_{eff}	kN	-7840	25.7	87.2	137	14.8	66.2	122
δ/D_s	-	0.416	0.920	2.39	3.73	0.64	1.97	3.50
# inc.	-	1	1	1	100	1	1	100
# sinus	-	220	220	220	220	220	220	420
Time	s	0.21	0.21	0.20	2.57	0.20	0.20	10.15

* The indicated frequency represents shear mode, see discussion in Section 6.1

Table C.3 – Input data and comparison of results from FE and semi-analytical method for verification cases 15-18.

Input	Unit	Case 15	Case 16	Case 17	Case 18
L_s	m	50	50	50	60
$L_{shoulder}$		150	150	150	180
L_{elem}		0.01683	0.01683	0.01683	0.01683
K_{VS}	MN/m^2	1.35	1.35	1.35	1.35
K_V		30.6	30.6	30.6	30.6
K_L, K_{AX}		23.0	23.0	23.0	23.0
D_s	m	0.1683	0.1683	0.1683	0.1683
t_s	m	0.0183	0.0183	0.0183	0.0183
q	N/m	664.1	664.1	664.1	664.1
m_e	kg/m	90.5	90.5	90.5	90.5
$S_{eff,i}$	kN	0	-25	-50	0
E	GPa	207	207	207	207
ν	-	0.29	0.29	0.29	0.29
Results, FE					
$f_{IL,1}$	Hz	0.553	0.542	0.531	0.474
$f_{IL,2}$		1.238	1.219	1.201	1.023
$f_{IL,3}$		2.133	2.109	2.086	1.698
$f_{CF,1}$		1.242	1.223	1.205	1.026
$f_{CF,2}$		1.492	1.534	1.575	1.388
$f_{CF,3}$		2.179	2.167	2.160	1.723
$A_{IL,1}$	MPa	33.5	33.0	31.8	27.5
$A_{IL,2}$		78.2	77.6	75.1	61.5
$A_{IL,3}$		134.9	134.3	130.3	103.9
$A_{CF,1}$		79.8	79.2	76.7	63.4
$A_{CF,2}$		89.8	102.6	110.6	89.0
$A_{CF,3}$		105.9	97.9	89.5	77.6
S_{eff}	kN	171	160	151	210
δ/D_s	-	5.09	5.31	5.53	6.70
Time	s	271.1	287.9	314.4	291.1
Results, Semi-Analytical					
$f_{IL,1}$	Hz	0.552	0.541	0.529	0.474
$f_{IL,2}$		1.239	1.219	1.200	1.023
$f_{IL,3}$		2.139	2.114	2.090	1.702
$f_{CF,1}$		1.244	1.224	1.205	1.026
$f_{CF,2}$		1.486	1.527	1.567	1.381
$f_{CF,3}$		2.185	2.172	2.162	1.724
$A_{IL,1}$	MPa	33.2	32.9	32.4	27.3
$A_{IL,2}$		77.5	77.3	76.4	61.2
$A_{IL,3}$		133.2	133.8	131.9	102.9
$A_{CF,1}$		79.0	78.8	77.8	62.1
$A_{CF,2}$		86.5	99.8	109.2	83.8
$A_{CF,3}$		105.8	98.7	93.9	77.3
S_{eff}	kN	168	158	148	207
δ/D_s	-	5.06	5.28	5.49	6.66
# inc.	-	100	100	100	100
# sinus	-	420	520	420	420
Time	s	10.74	16.98	11.49	11.12